COPPE
Instituto Alberto Luiz Coimbra de Pós-Graduação e Pesquisa de Engenharia
UFRJ

IMPACT OF DAMPER SEAL COEFFICIENTS IN ROTOR DYNAMICS: UNCERTAINTIES AND OPTIMIZATION

Raphael Timbó Silva

Dissertação de Mestrado apresentada ao Programa de Pós-graduação em Engenharia Mecânica, COPPE, da Universidade Federal do Rio de Janeiro, como parte dos requisitos necessários à obtenção do título de Mestre em Engenharia Mecânica.

Orientador: Thiago Gamboa Ritto

Rio de Janeiro
Outubro de 2018

IMPACT OF DAMPER SEAL COEFFICIENTS IN ROTOR DYNAMICS: UNCERTAINTIES AND OPTIMIZATION

Raphael Timbó Silva

DISSERTAÇÃO SUBMETIDA AO CORPO DOCENTE DO INSTITUTO ALBERTO LUIZ COIMBRA DE PÓS-GRADUAÇÃO E PESQUISA DE ENGENHARIA (COPPE) DA UNIVERSIDADE FEDERAL DO RIO DE JANEIRO COMO PARTE DOS REQUISITOS NECESSÁRIOS PARA A OBTENÇÃO DO GRAU DE MESTRE EM CIÊNCIAS EM ENGENHARIA MECÂNICA.

Examinada por:

Prof. Thiago Gamboa Ritto, D.Sc.

Prof. Daniel Alves Castello, D.Sc.

Prof. Aldemir Aparecido Cavalini Jr., D.Sc.

RIO DE JANEIRO, RJ – BRASIL
OUTUBRO DE 2018

Silva, Raphael Timbó

Impact of damper seal coefficients in rotor dynamics: uncertainties and optimization/Raphael Timbó Silva. – Rio de Janeiro: UFRJ/COPPE, 2018.

XV, 69 p.: il.; 29, 7cm.

Orientador: Thiago Gamboa Ritto

Dissertação (mestrado) – UFRJ/COPPE/Programa de Engenharia Mecânica, 2018.

Referências Bibliográficas: p. 60 – 64.

1. Compressor. 2. Rotordynamics. 3. Uncertanties. I. Ritto, Thiago Gamboa. II. Universidade Federal do Rio de Janeiro, COPPE, Programa de Engenharia Mecânica. III. Título.

Agradecimentos

Primeiramente, gostaria de agradecer ao meu orientador, Prof. Thiago Ritto, pela oportunidade de realizar este trabalho. Agradeço também por todos os ensinamentos e pela confiança depositada em mim.

Agradeço aos professores que tive na UFRJ durante esse período e também aos professores da minha graduação na UnB, especialmente aos professores Jorge e Pimenta por serem exemplos de pessoas nas quais me inspiro.

Também agradeço aos meus colegas de trabalho: Renner, Mancuzo, Letícia Tapajoz, Rodrigo e Leonardo Ishimoto pela amizade e ajuda neste trabalho. Joilson, por toda a ajuda e confiança no início da minha carreira profissional. Leandro Zague, pelo companheirismo principalmente durante a fase difícil do mestrado.

Gostaria também de agradecer à Petrobras, especialmente ao meu amigo Gustavo Levin, por me dar a oportunidade de me capacitar cada vez mais.

Agradeço a pessoas como Guido van Rossum, Travis Oliphant, Lorena Barba, Jason K. Moore, dentre tantos outros que trabalham para que código e ciência sejam abertos e acessíveis para todos.

Agradeço aos meus amigos de faculdade, especialmente André e Dieggo por tudo que pude aprender durante os anos de república.

Aos amigos da minha cidade Taguatinga, especialmente Harmson, Guilherme, Leonardo, Thiago, Marcos e Rivago que sei que mesmo com a distância irei sempre ter a amizade de todos.

Agradeço a minha família por todo o carinho e aos meus pais por terem sempre batalhado pela minha educação e dos meus irmãos.

Finalmente agradeço à minha companheira Luciana, por todo amor, carinho e compreensão ao longo desta jornada.

Resumo da Dissertação apresentada à COPPE/UFRJ como parte dos requisitos necessários para a obtenção do grau de Mestre em Ciências (M.Sc.)

IMPACTO DOS COEFICIENTES DO SELO AMORTECEDOR NA DINÂMICA DE ROTORES: INCERTEZAS E OTIMIZAÇÃO

Raphael Timbó Silva

Outubro/2018

Orientador: Thiago Gamboa Ritto

Programa: Engenharia Mecânica

Os selos amortecedores podem ter grande impacto na dinâmica de rotores, mas o cálculo dos valores dos coeficientes de rigidez e amortecimento para este componente é difícil e possui grande incerteza. No presente trabalho, um modelo probabilístico é proposto para modelar os coeficientes do selo, que são dependentes da frequência. Um processo estocástico (indexado na frequência) é construído de forma que o erro do modelo seja levado em consideração. O impacto dessas incertezas no comportamento rotodinâmico de um compressor é analisado. Os coeficientes determinísticos do selo são determinados considerando o modelo 'bulk-flow' e valores calculados por um fabricante de compressores baseado em uma extrapolação de dados experimentais. Os resultados obtidos mostram que a incerteza desses coeficientes tem um impacto considerável no comportamento rotodinâmico do compressor, afetando a margem de estabilidade e a resposta ao desbalanceamento. Baseado nesta análise, um procedimento para a otimização robusta do comportamento rotodinâmico do compressor é proposto. Este procedimento considera parâmetros geométricos do selo como variáveis de projeto. Os resultados da otimização robusta mostram que o comprimento do selo e a profundidade das células podem ser alterados com o objetivo de se obter uma melhor resposta ao desbalanceamento.

Abstract of Dissertation presented to COPPE/UFRJ as a partial fulfillment of the requirements for the degree of Master of Science (M.Sc.)

IMPACT OF DAMPER SEAL COEFFICIENTS IN ROTOR DYNAMICS: UNCERTAINTIES AND OPTIMIZATION

Raphael Timbó Silva

October/2018

Advisor: Thiago Gamboa Ritto

Department: Mechanical Engineering

Damper seals can have a significant impact on rotor dynamics, but the calculation of the stiffness and damping coefficients for this component can be challenging and has a high uncertainty. In the present work, a probabilistic model is proposed to model the seal coefficients, which are frequency-dependent. We develop a stochastic process (frequency indexed) so that the uncertainty in the model is taken into account. The impact of these uncertainties on the rotordynamic behavior of a compressor is analyzed. The deterministic coefficients of the seal are determined considering a bulk-flow model and values calculated by a compressor vendor based on the extrapolation of experimental data. The obtained results show that the uncertainty of these coefficients have a considerable impact on the compressor rotordynamic behavior, affecting the stability margin and the unbalance response. Based on this analysis, a procedure for the robust optimization of the compressor rotordynamic behavior is proposed. This procedure considers the seal geometric parameters as design variables. The results for the robust optimization show that the seal length and the cell hole depth can be modified to improve the unbalance response.

Contents

List of Figures

List of Tables

List of Symbols

A_e	element cross sectional area, p. 18
E_e	Young's modulus, p. 16
F	random interpolation factor, p. 33
G_e	shear modulus, p. 16
H	seal clearance, p. 28
H_d	cell hole depth, p. 28
I_d	diametral moment of inertia, p. 22
I_e	second moment of area, p. 21
I_p	polar moment of inertia, p. 21
N_{ei}	shape functions, p. 17
N_{ma}	minimum allowable speed - RPM, p. 8
N_{mc}	maximum continuous speed - RPM, p. 8
P	pressure, p. 29
Q_0	minimum cross coupling required to produce a zero log decrement, p. 11
Q_A	anticipated cross coupling, p. 10
R	seal radius, p. 28
R_g	gas constant, p. 29
T	period of oscillation, p. 11
T	temperature, p. 29
T_e	element kinetic energy, p. 18

U	circumferential bulk fluid velocity, p. 28
U_a	Input unbalance for the rotordynamic response analysis, $g{\cdot}mm$, p. 8
U_e	element strain energy, p. 18
U_r	maximum allowable residual unbalance, $g \cdot mm$, p. 8
V	radial bulk fluid velocity, p. 28
W	axial bulk fluid velocity, p. 28
W_j	journal static load in kg, p. 8
Ω	rotor precession frequency, p. 25
Ω_w	gas whirl precession frequency, p. 25
α_i	factor to determine weight for mean and variance, p. 35
β_e	angle between the plane of the beam cross-section, p. 15
β_i	weight factors for specific objective functions, p. 35
δ	logarithimic decrement, p. 11
δ_a	minimum log decrement at the anticipated cross coupling, p. 11
δ_f	log decrement of the complete rotor support system from the level 2 analysis, p. 11
γ_c	ratio between the area covered by cells and the seal total area, p. 29
κ_e	beam shear constant, p. 16
λ	ratio between gas whirl and rotor precession frequency, p. 25
$\mathbf{C}$	system damping matrix, p. 30
$\mathbf{G_e}$	element gyroscopic matrix, p. 22
$\mathbf{G}$	system gyroscopic matrix, p. 30
$\mathbf{K}$	system stiffness matrix, p. 30
$\mathbf{K}_e$	element stiffness matrix, p. 18

$\mathbf{M}$	system mass matrix, p. 30
$\mathbf{M}_e$	element mass matrix, p. 19
$\mathcal{C}$	damping random matrix, p. 33
$\mathcal{K}$	stiffness random matrix, p. 33
μ_e	ratio of the inner shaft radius to the outer shaft radius, p. 16
ν_e	Poisson's ratio, p. 16
ω_d	damped natural frequency, p. 11
ω_i	i-th natural frequency, p. 31
ω_n	natural frequency, p. 11
ω_{di}	i-th damped natural frequency, p. 31
ψ_e	angle of the Timoshenko beam cross section, p. 15
ρ_e	density of the material, p. 18
τ	wall-shear stress, p. 27
ξ_e	exit recovery factor, p. 30
ξ_i	inlet loss factor, p. 30
ζ	damping ratio, p. 11
ζ_i	i-th natural frequency, p. 31
c	cell to volume area ratio, p. 29
f	interpolation factor, p. 32
f_i	specific objective function, p. 35
l_e	beam length, p. 16
m	empirical friction factor constant, p. 27
m_d	disk mass, p. 22
n	empirical friction factor constant, p. 27
u_e	lateral displacement, p. 15
z_c	compressibility factor, p. 29

List of Abbreviations

CFD	Computational Fluid Dynamics, p. 6
CSR	Critical Speed Ratio, p. 11
DE	Drive-End side, p. 46
NDE	Non-Drive-End side, p. 35
TEHD	Thermo-elastohydrodynamic, p. 23

Chapter 1

Introduction

1.1 Motivation

Centrifugal compressors can be used to reinject gas during the oil production. This reinjection is done to maintain the pressure of the oil reservoir and also to store gas that cannot be exported.

The high pressure in which these compressors operate can lead to stability issues. Seals such as the honeycomb and hole-pattern can be used to increase the damping in the rotor, to this reason these are commonly referred as damper seals.

The damper seal has a high damping coefficient, but it can also have high stiffness. These coefficients can be of the same order of the bearing's coefficients and can affect the natural frequencies and the equipment's unbalance response.

The current standard for centrifugal compressors in the oil & gas industry (API 617 [1]) does not require the damper seal to be considered in the unbalance response analysis and its impact in this regard can go unnoticed until the equipment starts operating.

Even when the analyst considers this component, there are many uncertainties regarding the values of damping and stiffness coefficients, since experimental data to validate codes used to perform their calculation are still limited to relatively low pressure and density.

1.2 Dissertation Goals

The goals of this dissertation are the following:

- To study how uncertainties on damper seal's coefficients can influence the rotordynamic behavior;
- To propose a methodology to optimize unbalance response while keeping a safe stability margin using the seal geometry as a design parameter.

1.3 Centrifugal Compressors

Centrifugal compressors are widely used in the oil & gas industry in processes such as gas field operations, hydrocarbon and chemical processing. Their primary purpose is to increase gas flow pressure to the levels required by the process or to provide pressure differences to overcome system resistances, thus enabling gas flow through pipes and equipment LÜDTKE [6].

Centrifugal compressors are assembled in one or more sections. A section has defined external process conditions and consists of a series of stages. Figure 1.1 shows a compressor stage. The gas enters the impeller, which is the part responsible for transferring the shaft mechanical energy to an increase in pressure, temperature, and velocity. In the diffuser, the gas velocity decreases, resulting in a further increase in pressure and temperature. The return bend (or crossover bend) is responsible for changing the flow direction to the next stage. In the return channel deswirling of the gas occurs before entering the next impeller, since the gas swirling would impact the capacity of the next impeller to transfer energy to the gas.

The dotted red lines in fig. 1.1 show the interstage leakage, which is usually controlled by the use of labyrinth seals. These seals can exert forces on the rotor leading to instability, especially if swirling of the gas is not controlled before the seal entrance.

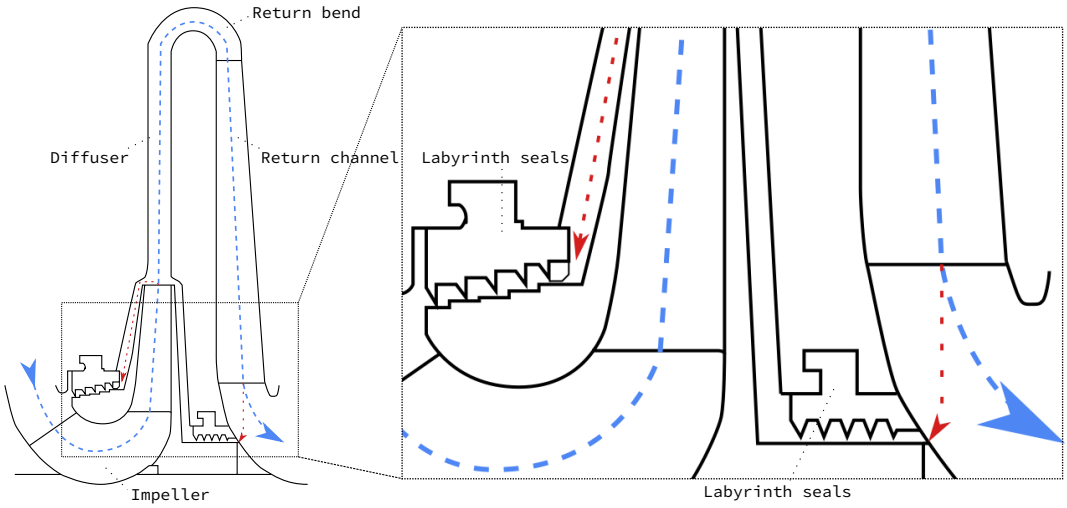

Figure 1.1: Compressor stage comprised by the impeller, return bend, return channel and interstage seals.

In the gas field operations, centrifugal compressors can be used in the exportation of produced gas, increasing of the oil production through gas lift or in the reinjection of gas to maintain the pressure of the oil reservoir and also to store gas that cannot be exported.

Reinjection of gas into the oil field can require a discharge pressure of more than

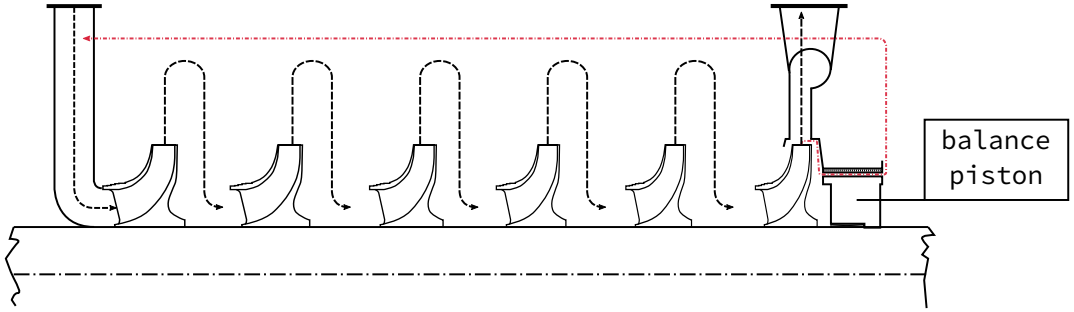

Figure 1.2: Inline compressor.

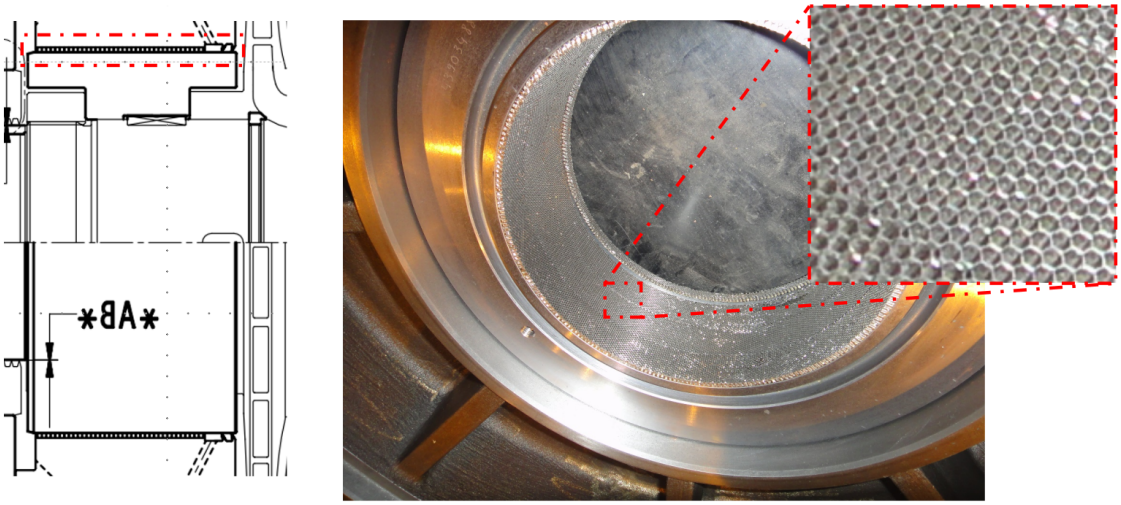

Figure 1.3: Honeycomb seal installed at the balance piston.

300 bar depending on the particular oil field. In some oil fields in which Petrobras operates this pressure can reach more than 550 bar with a high CO2 content which increases gas density, leading to a condition where we may have stability issues since the forces exerted by the seals are proportional to the gas pressure and density.

The high-pressure compressors used for reinjection can have one section with an 'in-line' (or straight-through) arrangement as shown in fig. 1.2, where the gas enters in the left and is compressed in each stage before being discharged at the right end side.

At the right end of the rotor, part of the gas goes to the discharge and part goes through the balance piston and back to the suction (dotted red line). For an in-line compressor, the balance piston helps to compensate the axial thrust caused by the impeller, decreasing the size of the required thrust bearing. The damper seal is installed in the balance piston and can have a honeycomb surface as illustrated in fig. 1.3. The design of this seal will be explained later.

In a back-to-back design, the compressor has two sections, gas enters the first section at the left end and is discharged after the third stage. Then the gas enters

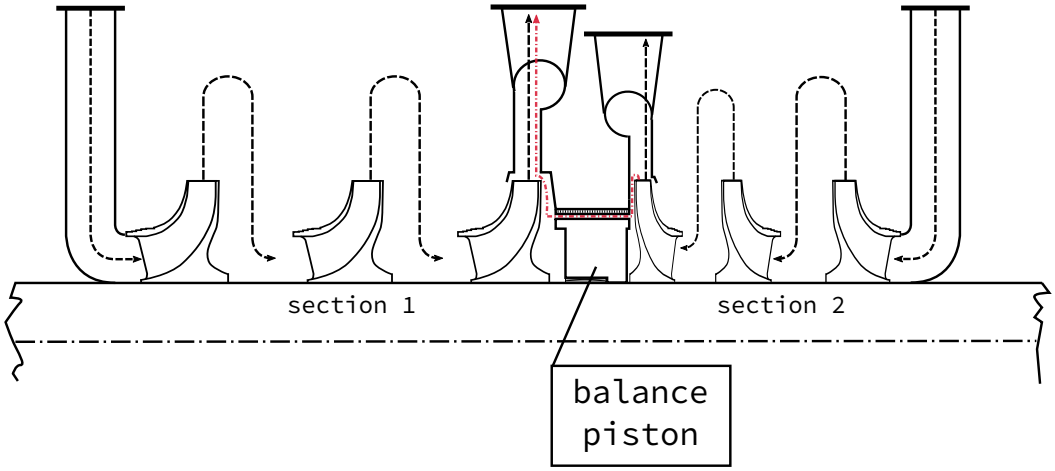

Figure 1.4: Back-to-back compressor.

the second section at the right end and is discharged at the middle. In this case, gas flows through the balance piston coming from the second section discharge to the first section discharge.

In a back-to-back compressor, the impellers arrangement balances most of the axial load.

There are several types of seals that can be used in the balance piston such as labyrinth, honeycomb, hole-pattern and pocket seals.

Labyrinth seals can have high cross-coupled stiffness terms that can make the rotor unstable. Honeycomb seals are commonly used on high-pressure compressors due to their stabilizing effect. According to VANNINI *et al.* [7] these seals also have a high cross-coupled term, but their damping coefficient is much higher than the labyrinth seals, resulting in a better overall effect on stability.

One point of great concern is that the damper seal has high stiffness, which can affect the critical speed position, its mode shape and the overall equipment's unbalance response. As mentioned by CHILDS and VANCE [8] this higher stiffness has been observed as shifts in critical speeds of compressors retrofitted with honeycomb seals. This change can lead to vibration problems at the site. A case is related by NORONHA *et al.* [9], in which a compressor presented high sensitivity to unbalance when the discharge pressure was increased and the seal started to act. In this case, the manufacturer had to change the damper seal design in order to decrease stiffness, move the critical speed and improve the unbalance response.

1.4 Damper Seal's Development

Around the mid-1970's, annular seals had the primary function of restricting gas leakage flow and were not considered important in rotordynamic. This lack of importance was because, when compared to the bearings, forces produced by these components were not considered relevant (CHILDS and VANCE [8]).

As described by VANNARSDALL [10], the push to achieve higher efficiency led to the application of methods such as:

1. Decrease the seal clearance to reduce leakage, which in turn increases the force generated in the seal;

2. Increase the operational speed, which raises the operational speed above the first critical and increases circumferential flow velocity;

3. Increase the working pressure and thereby the fluid density. Seal forces are proportional to pressure and density;

4. Adding stages to the machine thereby increasing the bearing span length and lateral vibration amplitudes.

With the development of these methods, the first cases of instability started to be reported. One of the most known cases is the Ekofisk compressor instability, which was reported at the time by GEARY JR *et al.* [11] as "subsynchronous rotor whirl" .

Although honeycomb (HC) seals have been used before in applications where these seals would be more resilient to the fluid (VANNARSDALL [10]), the first proposal of using seals to increase damping came from VON PRAGENAU [12], which proposed a seal surface roughness for stabilization and sealing for use in the fuel and oxidizer pumps of the space shuttle main engine.

The interest in these seals for rotordynamic application started to grow, and studies for predicting their behavior were carried out. However, as stated by VANNARSDALL [10], while HC seals can be superior to labyrinth seals regarding their rotordynamic performance and leakage characteristics, their behavior was erratic and hard to predict.

1.5 Available Data and Uncertainties on Damper Seal Coefficients

Typically, the software used to predict seal's coefficients use bulk-flow theory (which will be explained in the modeling section), with empirical friction factor, but a full

computational fluid dynamics (CFD) analysis can also be carried out to obtain these coefficients (NORONHA *et al.* [9]).

Unfortunately, experimental data to validate the numerical code are limited when we consider recent applications in which the pressure level (550 bar) and the high CO2 content can significantly increase the density.

CHILDS *et al.* [13] presented experimental results for leakage and rotordynamic coefficients for seven honeycomb seals. The test fluid was air, with a pressure up to approximately 8 bar and rotor speed reaching 16 000 RPM.

HA and CHILDS [14] presented results for experiments that used flat-plates to measure the friction factor for the damper seal surfaces. This work tested 36 different honeycomb surfaces and three smooth surfaces. The honeycomb surfaces showed a higher friction factor and a phenomenon named as 'friction factor jump' was identified. The friction factor is normally expected to keep constant with increasing Reynolds number when we consider a turbulent flow in a pipe, but in this case, the friction factor would suddenly present an increase when increasing the Reynolds number. This 'friction factor jump' was later attributed to acoustic phenomena.

HOLT and CHILDS [15] presented experimental results for two hole-pattern-stator seals and one smooth bore seal. Excitation-frequency range was 40 to 230 Hz; top running speed was 20200 RPM and the highest discharge pressure 17.2 bar. They used air as the test fluid.

CHILDS and WADE [16] present results for hole-pattern seal with a supply pressure of 70 bar, three pressure ratios and speed up to 20 000 RPM with air as the test fluid.

WAGNER *et al.* [17] gives results for dynamic coefficients of impeller eye labyrinth seals in which a test rig with a maximum test pressure of 70 bar was used. This work is not directly related to damper seal but gives an idea of the available test apparatus at the time.

Experiments for a hole-pattern seal that had cells with a relatively high diameter were carried out by VANNARSDALL and CHILDS [18]. In these experiments, a test rig that could have an inlet pressure of 70 bar and speed up to 20 200 RPM was used.

VANNINI *et al.* [7] presents the development of a test rig with a maximum test pressure of 350 bar. The test gas is restricted to nitrogen. The work gives results for a long labyrinth seal with inlet pressure up to 200 bar.

Considering the lack of experimental data and also the level of accuracy for tools currently available, seal's coefficients can present a high level of uncertainty, and this can have an impact on the rotordynamic model. As an example, KOCUR *et al.* [19] conducted a survey among vendors, users, academics and consulting companies where the different rotordynamic coefficients predictions of the same journal bearings

and labyrinth seals led to different results, with predictions for the first forward mode ranging from 6000 RPM to 11 300 RPM and the log dec with magnitudes from -1 to +1.

Chapter 2

Rotordynamic analysis

The rotordynamic analysis required by API 617 [1] can be divided into two parts:

1. Damped unbalanced rotor response;
2. Stability analysis.

The requirements for each analysis will be discussed.

2.1 Damped Unbalanced Rotor Response

The first step in the unbalance response analysis is to determine the undamped critical speeds and their mode shapes. Before detailing the analysis, we describe the definition for the following terms:

- N_{ma} : Minimum allowable Speed, RPM - Is the lowest rotational speed at which the machine can operate. It is normally dependent on a separation margin from the first critical speed;
- N_{mc} : Maximum Continuous Speed, RPM - Is the highest rotational speed at which the machine, as-built and tested, is capable of continuous operation;
- U_r : Maximum allowable residual unbalance, $g \cdot mm$. Calculated as:

$$U_r = 6350\frac{W_j}{N_{mc}} \tag{2.1}$$

  where W_j is the equivalent mass to the journal static load in kg. Equation (2.1) and the factor 6350 is in mm/min and is equivalent to a ISO 1940 [20] balance grade of 0.7;

- U_a Input unbalance for the rotordynamic response analysis, $g \cdot mm$ - This unbalance correspond to $2 \cdot U_r$.

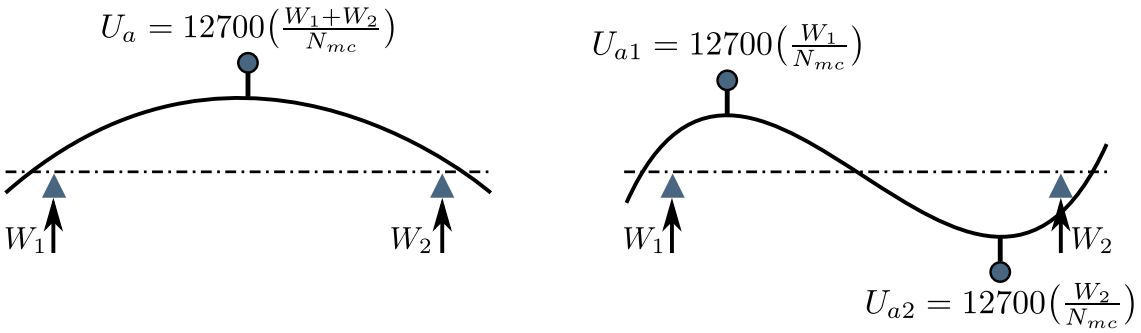

Figure 2.1: Typical mode shapes and corresponding unbalance API 617 [1].

For the critical speeds located within the speed range of 0 to 150 % of the N_{mc}, an unbalance U_a, corresponding to two times the maximum allowable residual unbalance U_r, shall be placed at the locations where they will cause the highest excitation. The unbalance placing is illustrated in fig. 2.1.

Two criteria shall be met in this analysis:

- Vibration at probe (sensor) location shall not exceed the defined vibration limit when operating over the range N_{ma} to N_{mc}. Vibration probes are usually located close to the bearings at both rotor ends;
- If, during the machine operation, the vibration at the probe location reaches the defined limit for the operational speed range, rotor displacement will not exceed 75 % of the minimum design diametral running clearance over the range from zero to trip speed. That means that, even when the machine is operating at the defined vibration limit, the rotor will be able to pass through critical speeds without presenting contact between rotating and stationary parts.

In the compressor's unbalance response analysis performed according to API 617 [1] item 4.8.2.4, the rotor is modeled considering a minimum of items that should be included. Some of these items are listed:

a) rotor stiffness, mass and polar and transverse moments of inertia;

b) bearing lubricant-film stiffness and damping values including changes due to speed, load, preload, oil inlet temperature, clearances, and the effect of asymmetrical loading such as gear forces, side streams, eccentric clearances and volutes;

c) for tilting-pad bearings, the pad pivot stiffness must be included;

d) structure stiffness, mass, and damping characteristics, including effects of excitation frequency over the required analysis range. For machines whose dynamic structural stiffness values are less than or equal to 3.5 times the bearing

stiffness values in the range from 0 to 150 % of N_{mc}, the structure characteristics shall be incorporated as an adequate dynamic system model;

e) rotational speed, including the various starting-speed detents, operating speed and load ranges.

Although the analysis is not limited to the listed items, *it is not required by the standard to include damper seal damping and stiffness characteristics* in the unbalance response evaluation.

According to API 617 [1] item 4.8.3, an unbalanced rotor response verification test shall be performed as part of the mechanical running test. This test is carried out by placing an unbalance weight at a previously defined rotor point (typically the coupling will be used due to the easy access). The machine will then be accelerated to the operating speed and the results, such as critical speed position and vibration amplitude, will be compared with those from the analysis report. If the test results are different from those encountered in the analysis, the vendor will have to review the analysis to meet the test results. If this review indicates that the machine is not according to the standard requirements a design change will be needed.

The problem with the unbalance response tests is that they are typically carried out close to no load condition due to contractual and financial reasons since a test on full load can be very expensive and sometimes prohibitive. In this case, the damper seal forces are not present due to the low gas pressure. This means that the test may not be representative when compared to the operating condition.

2.2 Stability Analysis

Stability analysis is divided into level 1 and level 2.

Level 1 analysis is an initial screening to identify rotors that do not require a detailed study. The items to be included are the same as those listed in section 2.1. We calculate an anticipated cross coupling Q_A based on conditions at the normal operating point. The cross-coupling is the force responsible for making the rotor unstable and it will be better explained in section 3.4. We also find the cross-coupling Q_0 required to produce a zero log decrement. These cross-coupling forces are inserted in the model as cross-coupled stiffness at a node located at the center of the rotor.

The real part of the eigenvalue can be used to verify the rotor stability, however API 617 [1] prefers to use the logarithimic decrement (log dec) for this evaluation. The log dec, denoted by δ is defined by:

$$\delta = \ln\left(\frac{x(t)}{x(t+T)}\right) \tag{2.2}$$

where T is the period of oscillation. Considering the analytical form of the undamped response this can be written as (INMAN [21]):

$$\delta = \ln\left(\frac{Ae^{-\zeta\omega_n t}\sin(\omega_d t + \phi)}{Ae^{-\zeta\omega_n (t+T)}\sin(\omega_d t + \omega_d T + \phi)}\right) \tag{2.3}$$

where ζ is the damping ratio, ω_n is the natural frequency and ω_d is the frequency of oscillation for the damped system.

Since $\omega_d T = 2\pi$, the expression reduces to:

$$\delta = \ln(e^{\zeta\omega_n T}) = \zeta\omega_n T \tag{2.4}$$

The period T in this case is the damped period $(2\pi/\omega_d)$ so that the log dec can be calculated from the damping ratio as:

$$\delta = \zeta\omega_n \frac{2\pi}{\omega_n\sqrt{1-\zeta^2}} = \frac{2\pi\zeta}{\sqrt{1-\zeta^2}} \tag{2.5}$$

The level 2 stability analysis will be required if any of the following apply:

1. $\dfrac{Q_0}{Q_A} < 2.0$;
2. $\delta_A < 0.1$, where δ_a is the minimum log decrement at the anticipated cross coupling;
3. $\dfrac{Q_0}{Q_A} < 10.0$ and the point defined by CSR and average gas density is located in Region B of fig. 2.2. CSR is the critical speed ratio and is defined as the ratio between the first critical speed and N_{mc}. API 617 [1] defines a critical speed as a speed at which the system is in a state of resonance.

For the level 2 stability analysis additional sources that contribute to the rotor stability shall be considered such as:

a) labyrinth seals;

b) damper seals;

c) impeller/blade flow aerodynamic effects;

d) internal friction.

The acceptance criterion is that the final log decrement, δ_f, shall be greater than 0.1.

As described above, the current standard requires the damper seals to be included only in the level 2 stability analysis, and its impact on the rotor unbalance response

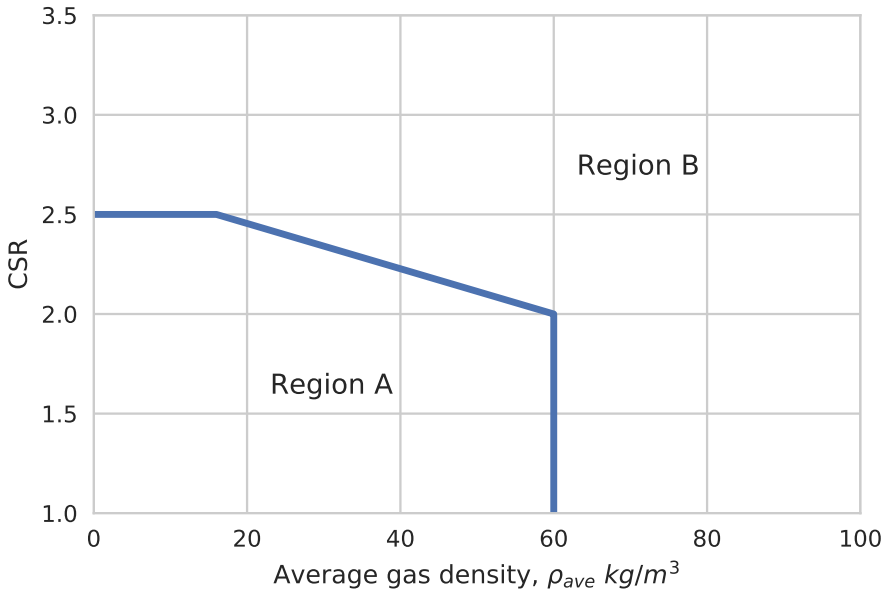

Figure 2.2: Stability experience plot API 617 [1].

is not evaluated. As shown in the next section, this component can have a significant impact on the unbalance response due to its high stiffness characteristics.

2.3 Damper Seals' Impact in the Rotor Response

In contrast with labyrinth seals with teeth, damper seals have a much higher direct stiffness. When the differential pressure across the damper seal is high, the magnitude of stiffness and damping synchronous coefficients associated with the seal may be in the same order of magnitude of the bearings' coefficients CHILDS and VANCE [8]. This characteristic has even led to researches to verify if this component could be used to replace oil lubricated bearings as described by RONDON [22]

Literature documents some cases relating different unbalance responses between no-load condition and operation in rated condition with high pressure and gas density.

BALDASSARRE and FULTON [23] show a case where a compressor with 237 bar discharge pressure presented high vibration during a full load test. Vibration varied between 6 µm to 25 µm as pressure and flow were varied, showing that the unbalance response was affected by the damper seal.

BALDASSARRE *et al.* [24] give as an example a back-to-back compressor with a damper seal installed at mid-span. The compressor operates with 300 bar of discharge pressure. A comparison is made between the critical speed map (Campbell diagram) in the no-load and full-load cases. The no-load case has the first critical speed around 6500 RPM with the second mode well above the operational speed. The damper seal impacts the rotor response, with the first mode frequency increasing with the speed after 7000 RPM. This behavior is mentioned by BALDASSARRE *et al.* [24] as 'tracking'.

A vibration issue for a compressor operating at 200 bar of discharge pressure is presented by NORONHA *et al.* [9]. Figure 2.3 shows how the vibration was related to the discharge pressure. The damper seal stiffness would increase with the pressure changing the first critical position and also the mode shape. In this case, the problem was detected only during operation, resulting in losses to the oil and gas production. Around August 2013 a modified seal was installed, and the vibration decreased to acceptable levels.

In BALDASSARRE *et al.* [25] two compressor units were evaluated. Unit 'A', which is similar to the compressor that will be evaluated at this dissertation, presents a considerable change in vibration when the compressor is operating on full load condition. As an example, when the suction pressure was increased from 200 bar to 250 bar Unit 'A' presented an increase in vibration three times higher than Unit 'B'.

According to the current API 684 [26], unbalance response is evaluated without consideration for the seal effects. BALDASSARRE *et al.* [24] provides steps for carrying out this kind of evaluation and proposes a specific acceptance criterion based on a generalization of the API approach.

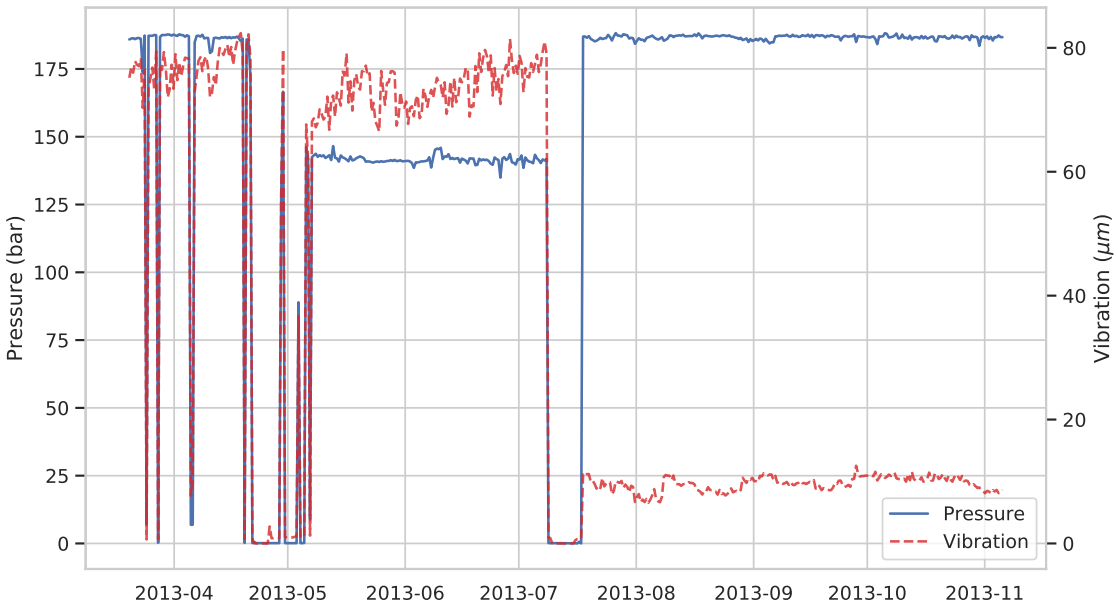

Figure 2.3: Increase on vibration related to discharge pressure.

Chapter 3

Modeling

This section will present the mathematical modeling of the rotor parts that were considered when developing the code used in the current work.

3.1 Shaft

For the shaft elements, shear and rotary inertia effects will be considered (Timoshenko beam model). Figure 3.1 shows the effect of shear through an angle β_e, which is the difference between the plane of the beam cross-section and the normal to the beam centerline (FRISWELL [2]).

The angle of the beam cross section, ψ_e, is:

$$\psi_e(\xi, t) = \frac{\partial u_e(\xi, t)}{\partial \xi} + \beta_e(\xi, t) \tag{3.1}$$

where u_e is the lateral displacement.

For a symmetric shaft, if effects like internal damping and axial torque are neglected we can consider that the two bending planes are uncoupled so that forces and moments in one plane cause displacements and rotations only in the same plane.

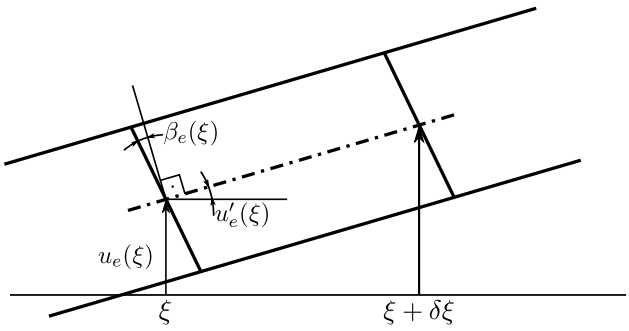

Figure 3.1: Small section of a Timoshenko beam (adapted from FRISWELL [2]).

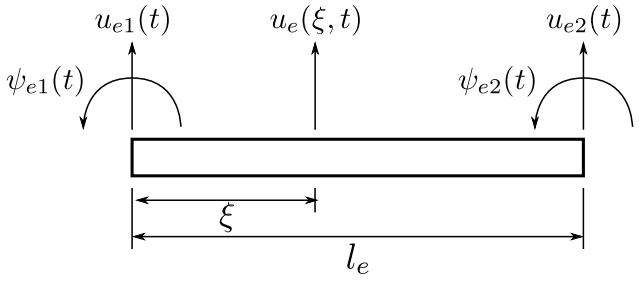

Figure 3.2: Coordinates for beam element (adapted from FRISWELL [2]).

With this consideration we can solve separately for each plane. Based on coordinates shown in fig. 3.2 we have:

$$\psi_{e1}(t) = \left.\frac{\partial u_e}{\partial \xi}\right|_{\xi=0} + \beta_e(0,t) \tag{3.2}$$

$$\psi_{e2}(t) = \left.\frac{\partial u_e}{\partial \xi}\right|_{\xi=l_e} + \beta_e(l_e,t) \tag{3.3}$$

where l_e is the beam length.

The lateral displacement, u_e, is assumed to be cubic:

$$u_e(\xi,t) = a_o(t) + a_1(t)\xi + a_2(t)\xi^2 + a_3(t)\xi^3 \tag{3.4}$$

Neglecting inertia terms, the shear angle, β_e, can be related to the lateral displacement, u_e, considering the moment equilibrium as:

$$\frac{\partial}{\partial \xi}\left(E_e I_e(\xi)\frac{\partial \psi_e(\xi,t)}{\partial \xi}\right) = \kappa_e G_e A_e \beta_e(\xi,t) \tag{3.5}$$

where κ_e is the shear constant that depends on the shape of the cross section of the beam and G_e is the shear modulus, with $G_e = E_e/2(1+\nu_e)$, where E_e is the Young's modulus and ν_e is Poisson's ratio.

The shear constant κ_e is used to compensate the stiffening effect of the assumption that plane sections remain plane. COWPER [27] gives values of the shear constant for typical cross sections. For a hollow, circular shaft section, the shear constant can be calculated as:

$$\kappa_e = \frac{6(1+\nu_e)(1+\mu_e^2)^2}{(7+6\nu_e)(1+\mu_e^2)^2 + (20+12\nu_e)\mu_e^2} \tag{3.6}$$

where μ_e is the ratio of the inner shaft radius to the outer shaft radius, $\mu_e = r_i/r_o$.

Substituting equation eq. (3.1) into eq. (3.5) we have:

$$\frac{\partial^2 \beta_e(\xi,t)}{\partial \xi^2} + \frac{\partial^3 u_e(\xi,t)}{\partial \xi^3} = \frac{\kappa_e G_e A_e}{E_e I_e}\beta_e(\xi,t) \tag{3.7}$$

The solution for this equation is a constant shear angle β_e approximated by

$$\beta_e(\xi,t) = \frac{\Phi_e l_e^2}{12}\frac{\partial^3 u_e(\xi,t)}{\partial \xi^3} \tag{3.8}$$

where

$$\Phi_e = \frac{12 E_e I_e}{\kappa_e G_e A_e l_e^2} \tag{3.9}$$

Applying conditions $u_e(0) = u_{e1}$ and $u_e(l_e) = u_{e2}$:

$$a_0 = u_{e1} \tag{3.10}$$

$$a_0 + a_1 l_3 + a_2 l_e^2 + a_3 l_3^3 = u_{e2} \tag{3.11}$$

Applying rotational nodal conditions eq. (3.2) and eq. (3.3):

$$a_1 + a_3\frac{\Phi_e l_e^2}{2} = \psi_{e1} \tag{3.12}$$

$$a_1 + 2a_2 l_e + a_3\left(3l_e^2 + \frac{\Phi_e l_3^2}{2}\right) = \psi_{e2} \tag{3.13}$$

Solving and grouping terms gives

$$u_e(\xi,t) = [N_{e1}(\xi)N_{e2}(\xi)N_{e3}(\xi)N_{e4}(\xi)]\begin{bmatrix} u_{e1}(t) \\ \psi_{e1}(t) \\ u_{e2}(t) \\ \psi_{e2}(t) \end{bmatrix} \tag{3.14}$$

where the shape functions, $N_{ei}(\xi)$, are

$$N_{e1}(\xi) = \frac{1}{1+\Phi_e}\left(1 + \Phi_e - \Phi_e\frac{\xi}{l_e} - 3\frac{\xi^2}{l_e^2} + 2\frac{\xi^3}{l_e^3}\right) \tag{3.15}$$

$$N_{e2}(\xi) = \frac{l_e}{1+\Phi_e}\left(\frac{2+\Phi_e}{2}\frac{\xi}{l_e} - \frac{4+\Phi_e}{2}\frac{\xi^2}{l_e^2} + \frac{\xi^3}{l_e^3}\right) \tag{3.16}$$

$$N_{e3}(\xi) = \frac{1}{1+\Phi_e}\left(\Phi_e\frac{\xi}{l_e} + 3\frac{\xi^2}{l_e^2} - 2\frac{\xi^3}{l_e^3}\right) \tag{3.17}$$

$$N_{e4}(\xi) = \frac{l_e}{1+\Phi_e}\left(-\frac{\Phi_e}{2}\frac{\xi}{l_e} - \frac{2-\Phi_e}{2}\frac{\xi^2}{l_e^2} + \frac{\xi^3}{l_e^3}\right) \tag{3.18}$$

The strain energy for the element is

$$U_e = \frac{1}{2}\int_0^{l_e} E_e I_e(\xi)\left(\frac{\partial \psi_e(\xi,t)}{\partial \xi}\right)^2 d\xi + \frac{1}{2}\int_0^{l_e} \kappa_e^2 G_e A_e(\xi)\beta_e^2(\xi,t)d\xi \tag{3.19}$$

Since β_e is constant across the length of the element with a uniform cross section:

$$\frac{\partial \psi_e(\xi,t)}{\partial \xi} = \frac{\partial^2 u_e(\xi,t)}{\partial \xi^2} + \frac{\partial \beta_e(\xi,t)}{\partial \xi} = \frac{\partial^2 u_e(\xi,t)}{\partial \xi^2} \tag{3.20}$$

Then:

$$U_e = \frac{1}{2}\begin{bmatrix} u_{e1}(t) \\ \psi_{e1}(t) \\ u_{e2}(t) \\ \psi_{e2}(t) \end{bmatrix}^T \begin{bmatrix} k_{11} & k_{12} & k_{13} & k_{14} \\ k_{21} & k_{22} & k_{23} & k_{24} \\ k_{31} & k_{32} & k_{33} & k_{34} \\ k_{41} & k_{42} & k_{43} & k_{44} \end{bmatrix} \begin{bmatrix} u_{e1}(t) \\ \psi_{e1}(t) \\ u_{e2}(t) \\ \psi_{e2}(t) \end{bmatrix} \tag{3.21}$$

where the stiffness matrix elements are

$$k_{ij} = E_e I_e \int_0^{l_e} N_{ei}''(\xi) N_{ej}''(\xi) d\xi + \frac{E_e I_e \Phi_e l_e^2}{12}\int_0^{l_e} N_{ei}'''(\xi) N_{ej}'''(\xi) d\xi \tag{3.22}$$

After the integration of each matrix element, the resulting stiffness matrix is

$$\mathbf{K}_e = \frac{E_e I_e}{(1+\Phi_e) l_e^3}\begin{bmatrix} 12 & 6l_e & -12 & 6l_e \\ 6l_e & l_e^2(4+\Phi_e) & -6l_e & l_e^2(2-\Phi_e) \\ -12 & -6l_e & 12 & -6l_e \\ 6l_e & l_e^2(2-\Phi_e) & 6l_e & l_e^2(4+\Phi_e) \end{bmatrix} \tag{3.23}$$

The kinetic energy for a shaft element is

$$T_e = \frac{1}{2}\int_0^{l_e} (\rho_e A_e \dot{u}_e^2 + \rho_e I_e \dot{\psi}_e^2) d\xi \tag{3.24}$$

$$= \frac{1}{2}\int_0^{l_e} \rho_e A_e \dot{u}_e^2 + \rho_e I_e \left(\dot{\beta}_e + \frac{\partial \dot{u}_e}{\partial \xi}\right)^2 d\xi \tag{3.25}$$

where ρ_e is the density of the material and A_e is the beam cross sectional area.

In terms of the mass matrix we have

$$T_e = \frac{1}{2}\begin{bmatrix} \dot{u}_{e1}(t) \\ \dot{\psi}_{e1}(t) \\ \dot{u}_{e2}(t) \\ \dot{\psi}_{e2}(t) \end{bmatrix}^T \begin{bmatrix} m_{11} & m_{12} & m_{13} & m_{14} \\ m_{21} & m_{22} & m_{23} & m_{24} \\ m_{31} & m_{32} & m_{33} & m_{34} \\ m_{41} & m_{42} & m_{43} & m_{44} \end{bmatrix} \begin{bmatrix} \dot{u}_{e1}(t) \\ \dot{\psi}_{e1}(t) \\ \dot{u}_{e2}(t) \\ \dot{\psi}_{e2}(t) \end{bmatrix} \tag{3.26}$$

For a uniform cross-sectional beam, the m_{ij} terms are

$$m_{ij} = \rho_e A_e \int_0^{l_e} N_{ei}(\xi) N_{ej}(\xi) d\xi + \rho_e I_e \int_0^{l_e} \left(\frac{\Phi_e l_e^2}{12} N_{ei}^{'''}(\xi) + N_{ei}^{'}(\xi) \right) \left(\frac{\Psi_e l_e^2}{12} N_{ej}^{'''}(\xi) + N_{ej}^{'}(\xi) \right) d\xi \tag{3.27}$$

Integrating the items we have the mass matrix:

$$\mathbf{M}_e = \frac{\rho_e A_e l_e}{840(1+\Phi_e)^2} \begin{bmatrix} m_1 & m_2 & m_3 & m_4 \\ m_2 & m_5 & -m_4 & m_6 \\ m_3 & -m_4 & m_1 & -m_2 \\ m_4 & m_6 & -m_2 & m_5 \end{bmatrix} + \frac{\rho_e I_e}{30(1+\Phi_e)^2 l_e} \begin{bmatrix} m_7 & m_8 & -m_7 & m_8 \\ m_8 & m_9 & -m_8 & m_{10} \\ -m_7 & -m_8 & m_7 & -m_8 \\ m_8 & m_{10} & -m_8 & m_9 \end{bmatrix} \tag{3.28}$$

where

$$m_1 = 312 + 588\Phi_e + 280\Phi_e^2 \tag{3.29}$$

$$m_2 = (44 + 77\Phi_e + 35\Phi_e^2) l_e \tag{3.30}$$

$$m_3 = 108 + 252\Phi_e + 140\Phi_e^2 \tag{3.31}$$

$$m_4 = -(26 + 63\Phi_e + 35\Phi_e^2) l_e \tag{3.32}$$

$$m_5 = (8 + 14\Phi_e + 7\Phi_e^2) l_e^2 \tag{3.33}$$

$$m_6 = -(6 + 14\Phi_e + 7\Phi_e^2) l_e^2 \tag{3.34}$$

$$m_7 = 36 \tag{3.35}$$

$$m_8 = (3 - 15\Phi_e) l_e \tag{3.36}$$

$$m_9 = (4 + 5\Phi_e + 10\Phi_e^2) l_e^2 \tag{3.37}$$

$$m_{10} = (-1 - 5\Phi_e = 5\Phi_e^2) l_e^2 \tag{3.38}$$

The second matrix represents the effect of rotary inertia.

Since we made the assumption that the two bending planes do not couple, the element matrices for the two planes are inserted in a 8 x 8 shaft element matrix considering the choice of coordinates shown in fig. 3.3, where we have the local coordinate vector $[u_1, v_1, \theta_1, \psi_1, u_2, v_2, \theta_2, \psi_2]^T$. The final 8x8 matrices are displayed

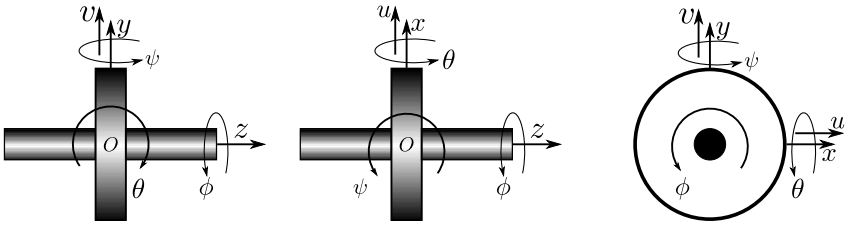

Axis Ox into paper | Axis Oy out of paper | Axis Oz out of paper

Figure 3.3: Coordinates used (adapted from FRISWELL [2]).

bellow for completeness.

$$\mathbf{M}_e = \frac{\rho_e A_e l_e}{840(1+\Phi_e)^2} \begin{bmatrix} m_1 & 0 & 0 & m_2 & m_3 & 0 & 0 & m_4 \\ 0 & m_1 & -m_2 & 0 & 0 & m_3 & -m_4 & 0 \\ 0 & -m_2 & m_5 & 0 & 0 & m_4 & m_6 & 0 \\ m_2 & 0 & 0 & m_5 & -m_4 & 0 & 0 & m_6 \\ m_3 & 0 & 0 & -m_4 & m_1 & 0 & 0 & -m_2 \\ 0 & m_3 & m_4 & 0 & 0 & m_1 & m_2 & 0 \\ 0 & -m_4 & m_6 & 0 & 0 & m_2 & m_5 & 0 \\ m_4 & 0 & 0 & m_6 & -m_2 & 0 & 0 & m_5 \end{bmatrix} \tag{3.39}$$

$$+ \frac{\rho_e I_e}{30(1+\Phi_e)^2 l_e} \begin{bmatrix} m_7 & 0 & 0 & m_8 & -m_7 & 0 & 0 & m_8 \\ 0 & m_7 & -m_8 & 0 & 0 & m_7 & -m_8 & 0 \\ 0 & -m_8 & m_9 & 0 & 0 & m_8 & m_{10} & 0 \\ m_8 & 0 & 0 & m_9 & -m_8 & 0 & 0 & m_{10} \\ -m_7 & 0 & 0 & -m_8 & m_1 & 0 & 0 & -m_8 \\ 0 & -m_7 & m_8 & 0 & 0 & m_7 & m_8 & 0 \\ 0 & -m_8 & m_{10} & 0 & 0 & m_8 & m_9 & 0 \\ m_8 & 0 & 0 & m_{10} & -m_8 & 0 & 0 & m_9 \end{bmatrix}$$

$$\mathbf{K}_e = \frac{E_e I_e}{(1+\Phi_e) l_e^3} \begin{bmatrix} 12 & 0 & 0 & 6l_e & -12 & 0 & 0 & 6l_e \\ 0 & 12 & -6l_e & 0 & 0 & -12 & -6l_e & 0 \\ 0 & -6l_e & l_e^2(4+\Phi_e) & 0 & 0 & 6l_e & l_e^2(2-\Phi_e) & 0 \\ 6l_e & 0 & 0 & l_e^2(4+\Phi_e) & -6l_e & 0 & 0 & l_e^2(2-\Phi_e) \\ -12 & 0 & 0 & -6l_e & 12 & 0 & 0 & -6l_e \\ 0 & -12 & 6l_e & 0 & 0 & 12 & 6l_e & 0 \\ 0 & -6l_e & l_e^2(2-\Phi_e) & 0 & 0 & 6l_e & l_e^2(4+\Phi_e) & 0 \\ 6l_e & 0 & 0 & l_e^2(2-\Phi_e) & -6l_e & 0 & 0 & l_e^2(4+\Phi_e) \end{bmatrix} \tag{3.40}$$

The shaft also produces gyroscopic effects. For a thin disk of thickness $d\xi$ the polar moment of inertia may be written as:

$$I_p = 2\rho_e I_e d\xi \tag{3.41}$$

where I_e is the second moment of area of the shaft about the neutral plane.

The increment in kinetic energy of this thin disk due to the rotation about a diameter is:

$$dT = -I_p \omega \dot{\psi}_e(\xi, t)\theta_e(\xi, t) = -2\rho_e I_e \omega \dot{\psi}_e(\xi, t)\theta_e(\xi, t)d\xi \tag{3.42}$$

where $\omega = \dot{\phi}$ is the rotational speed.

Integrating over the length gives the contribution to the kinetic energy as:

$$T_{Ge} = -2\rho_e I_e \omega \int_0^{l_e} \dot{\psi}_e(\xi, t)\theta_e(\xi, t)d\xi \tag{3.43}$$

The rotations may be written in terms of the shape functions:

$$\begin{aligned} \begin{bmatrix} \theta_e(\xi, t) \\ \psi_e(\xi, t) \end{bmatrix} &= \begin{bmatrix} 0 & -N_1' & N_2' & 0 & 0 & -N_3' & N_4' & 0 \\ N_1' & 0 & 0 & N_2' & N_3' & 0 & 0 & N_4' \end{bmatrix} \mathbf{q_e} \\ &= \begin{bmatrix} B_{11} & B_{13} & B_{13} & B_{14} & B_{15} & B_{16} & B_{17} & B_{18} \\ B_{21} & B_{23} & B_{23} & B_{24} & B_{25} & B_{26} & B_{27} & B_{28} \end{bmatrix} \mathbf{q_e} \end{aligned} \tag{3.44}$$

where the $\mathbf{B}$ terms are used for convenience.

Substituting equation eq. (3.44) into eq. (3.43) gives:

$$T_{Ge} = \dot{\mathbf{q}}_\mathbf{e}^T \mathbf{A} \mathbf{q_e} \tag{3.45}$$

where

$$A_{ij} = -2\rho_e I_e \omega \int_0^{l_e} B_{2i}(\xi)B_{1j}(\xi)d\xi \tag{3.46}$$

Then, from Lagrange's equations

$$\begin{bmatrix} \frac{d}{dt}\left(\frac{\partial T_{Ge}}{\partial \dot{q}_1}\right) - \frac{\partial T_{Ge}}{\partial q_1} \\ \vdots \\ \frac{d}{dt}\left(\frac{\partial T_{Ge}}{\partial \dot{q}_8}\right) - \frac{\partial T_{Ge}}{\partial q_8} \end{bmatrix} = [\mathbf{A} - \mathbf{A}^T]\dot{\mathbf{q}} = \omega \mathbf{G_e} \dot{\mathbf{q}} \tag{3.47}$$

Equation (3.46) gives the elements of the gyroscopic matrix as:

$$G_{ij} = -2\rho_e I_e \int_0^{l_e} (B_{2i}(\xi)B_{1j}(\xi) - B_{2j}(\xi)B_{1i}(\xi))d\xi \tag{3.48}$$

Carrying out the calculations gives the shaft gyroscopic matrix considering rotary inertia and shear effects:

$$\mathbf{G_e} = \frac{\rho_e I_e}{15(1+\Phi_e)^2 l_e}\begin{bmatrix} 0 & g_1 & -g_2 & 0 & 0 & -g_1 & -g_2 & 0 \\ -g_1 & 0 & 0 & -g_2 & g_1 & 0 & 0 & -g_2 \\ g_2 & 0 & 0 & g_3 & -g_2 & 0 & 0 & -g_4 \\ 0 & g_2 & -g_3 & 0 & 0 & -g_2 & -g_4 & 0 \\ 0 & -g_1 & g_2 & 0 & 0 & g_1 & g_2 & 0 \\ g_1 & 0 & 0 & g_2 & -g_1 & 0 & 0 & g_2 \\ g_2 & 0 & 0 & -g_4 & -g_2 & 0 & 0 & g_3 \\ 0 & g_2 & g_4 & 0 & 0 & -g_2 & -g_3 & 0 \end{bmatrix} \tag{3.49}$$

where

$$\begin{aligned} g_1 &= 36 \\ g_2 &= (3 - 15\Phi_e) l_e \\ g_3 &= (4 + 5\Phi + 10\Phi_e^2) l_e^2 \\ g_4 &= (-1 - 5\Phi_e + 5\Phi_e^2) l_e^2 \end{aligned} \tag{3.50}$$

3.2 Disk

For a disk, assuming the rotations θ and ψ are small, the kinetic energy is (FRISWELL [2])

$$T_d = \frac{1}{2} m_d (\dot{u}^2 + \dot{v}^2) + \frac{1}{2} I_d (\dot{\theta}^2 + \dot{\psi}^2) + \frac{1}{2} I_p (\omega^2 - 2\omega\dot{\psi}\theta) \tag{3.51}$$

where m_d is the mass of the disk, I_p, is the polar moment of inertia and I_d is the diametral moment of inertia about any axis perpendicular to the shaft line.

The terms from Lagrange's equations are

$$\begin{bmatrix} \frac{d}{dt}\left(\frac{\partial T_d}{\partial \dot{u}}\right) - \frac{\partial T_d}{\partial u} \\ \vdots \\ \frac{d}{dt}\left(\frac{\partial T_d}{\partial \dot{\psi}}\right) - \frac{\partial T_d}{\partial \psi} \end{bmatrix} = \begin{bmatrix} m_d & 0 & 0 & 0 \\ 0 & m_d & 0 & 0 \\ 0 & 0 & I_d & 0 \\ 0 & 0 & 0 & I_d \end{bmatrix} \begin{bmatrix} \ddot{u} \\ \ddot{v} \\ \ddot{\theta} \\ \ddot{\psi} \end{bmatrix} + \omega \begin{bmatrix} 0 & 0 & 0 & 0 \\ 0 & 0 & 0 & 0 \\ 0 & 0 & 0 & I_p \\ 0 & 0 & -I_p & 0 \end{bmatrix} \begin{bmatrix} \dot{u} \\ \dot{v} \\ \dot{\theta} \\ \dot{\psi} \end{bmatrix} \tag{3.52}$$

Then the mass matrix for the disk is

$$\mathbf{M}_e = \begin{bmatrix} m_d & 0 & 0 & 0 \\ 0 & m_d & 0 & 0 \\ 0 & 0 & I_d & 0 \\ 0 & 0 & 0 & I_d \end{bmatrix} \tag{3.53}$$

and the gyroscopic matrix is

$$\mathbf{G}_e = \begin{bmatrix} 0 & 0 & 0 & 0 \\ 0 & 0 & 0 & 0 \\ 0 & 0 & 0 & I_p \\ 0 & 0 & -I_p & 0 \end{bmatrix} \tag{3.54}$$

3.3 Bearings

It is assumed that the bearing has a linear load-deflection relationship. Thus, the relation between transverse forces acting on the shaft (f_x and f_y) transverse vibrations at the bearing positions (u and v) may be approximated by FRISWELL [2]:

$$\begin{bmatrix} f_x \\ f_y \end{bmatrix} = - \begin{bmatrix} K_{uu} & k_{uv} \\ k_{vu} & K_{vv} \end{bmatrix} \begin{bmatrix} u \\ v \end{bmatrix} - \begin{bmatrix} C_{uu} & c_{uv} \\ c_{vu} & C_{vv} \end{bmatrix} \begin{bmatrix} \dot{u} \\ \dot{v} \end{bmatrix} \tag{3.55}$$

where f_x and f_y are the dynamic forces in the x and y directions, and u and v are the displacements of the shaft journal relative to the bearing house in the x and y direction. Notice that in this work we will refer to direct terms in upper case letters (K_{uu}) and cross-coupled terms in lower case letters (k_{uv}).

The K_{uu} coefficient corresponds to the ratio between a force applied in the x direction and the displacement in the x direction. Since force and displacement are in the same direction, this coefficient is called a direct stiffness coefficient.

The k_{uv} coefficient corresponds to a force applied in the x direction and a displacement in the y direction. In this case, we have a cross-coupled stiffness coefficient.

The coefficients for the bearings were calculated using MAXBRG software, which is a finite element code that performs steady-state thermo-elastohydrodynamic (TEHD) analysis for fluid film journal bearings (HE [28]).

3.4 Damper Seal

The work of BLACK [29] (1969) is regarded as the first that analyzed the impact of seals on the rotordynamic behavior of turbomachinery. His work shows that

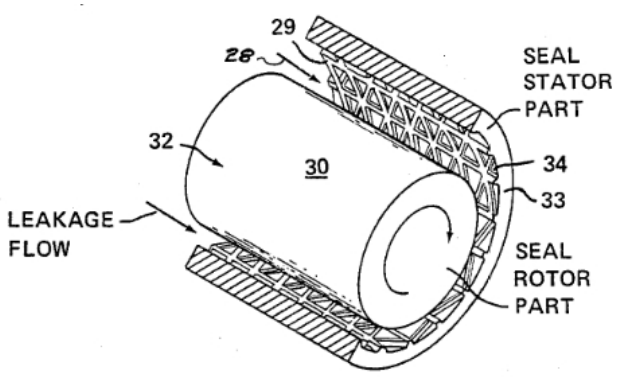

Figure 3.4: Damper seal with triangular pockets on seal stator part from VON PRAGENAU [3] patent.

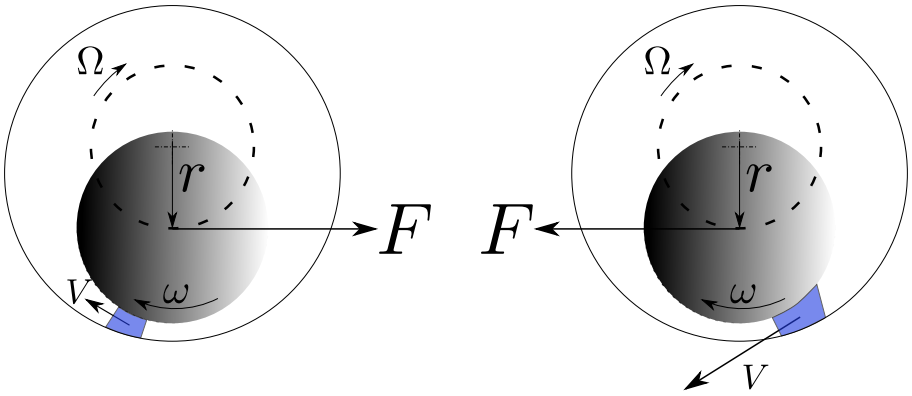

(a) Gas rotating slowly ($\lambda < 1$). (b) Gas rotating fast ($\lambda > 1$).

Figure 3.5: Gas rotating speed and its influence in the rotor stability.

instability at high speeds may result from forces caused by the rotation of the fluid in the seals.

CHILDS [30] (1978) evaluated the SSME (Space Shuttle Main Engine) HPFTP (High-Pressure Fuel Turbopump) rotordynamic instability problem, and suggested that the seal forces could be used to improve the rotor stability. VON PRAGENAU [12], based on models developed by BLACK *et al.* [31], proposed a stator with a high surface roughness relative to the rotor roughness to reduce fluid whirl and improve stability and leakage. In 1985 he also patented a damper seal with a surface of triangular pockets as shown in fig. 3.4.

The mechanism by which fluid whirl can induce instability is visually explained by BALDASSARRE *et al.* [25] and illustrated in section 3.4.

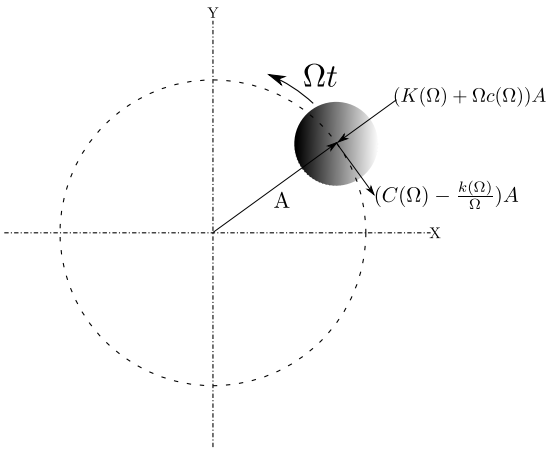

Figure 3.6: Precessing rotor with seal radial and circumferential force components.

Consider the following parameter:

$$\lambda = \frac{\Omega_w}{\Omega} \tag{3.56}$$

where Ω is the rotor precession (different from ω that is the rotor speed) and Ω_w is the gas whirl precession.

If $\lambda < 1$, the gas is rotating slower than the shaft orbit, and the rotor has to push the gas tangentially as a consequence of its radial displacement. Part of the rotor's kinetic energy is transferred to the gas and part is lost due to friction, so that the gas has a stabilizing effect.

If $\lambda > 1$, the gas is rotating faster than the rotor orbit, so that the shaft is pushed along the tangential direction by the gas. The rotor is gaining kinetic energy and the effect is destabilizing.

This destabilizing force is manifested through the cross-coupled stiffness term, which can be explained with the use of fig. 3.6, in which the radial and circumferential forces are displayed. The effective stiffness and the effective damping can be calculated as:

$$K_{eff} = (K(\Omega) + \Omega c(\Omega))A \tag{3.57}$$

$$C_{eff} = (C(\Omega) - \frac{k(\Omega)}{\Omega})A \tag{3.58}$$

where K and C are the direct terms, and k and c are the cross coupled terms for stiffness and damping respectively. As noticed above, the dynamic coefficients are frequency dependent. In this work we will consider synchronous coefficients, that is: $\Omega = \omega$ when calculating the coefficients.

As we can see, the effective damping, which is responsible for the rotor stability, is subtracted by the cross-coupled stiffness term. Therefore, a component that presents a high direct damping and a low cross-coupled stiffness will have a stabilizing effect

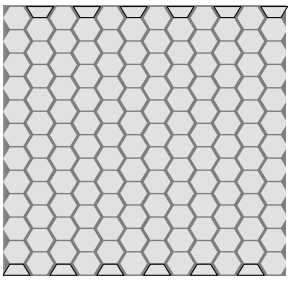

(a) Honeycomb surface.

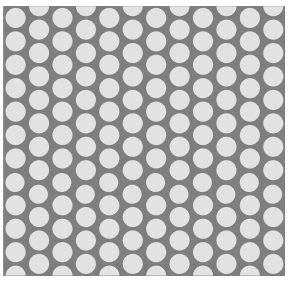

(b) Hole-pattern surface.

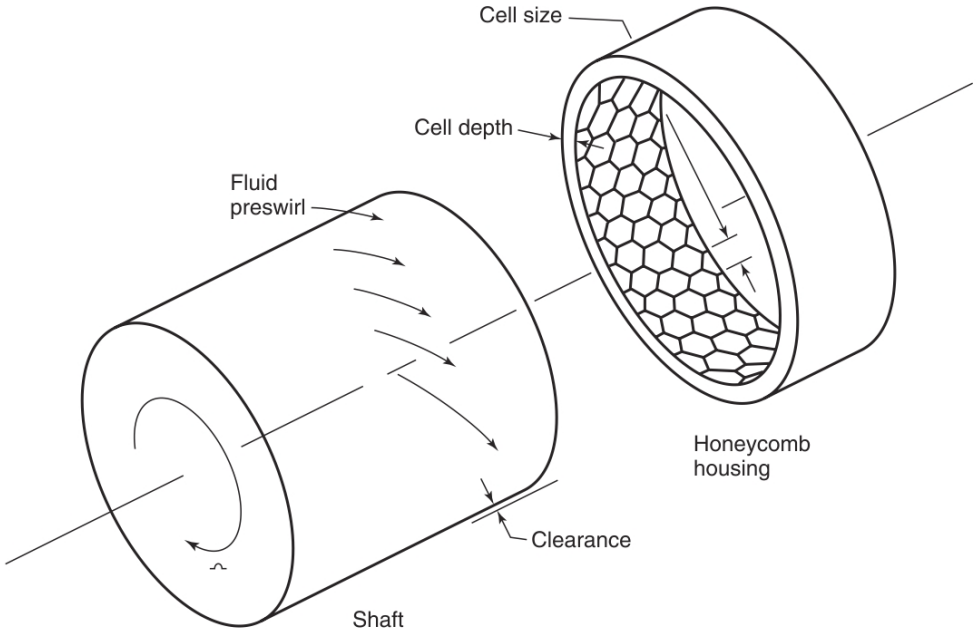

(c) Honey-comb seal CHILDS [32].

Figure 3.7: Damper seal and the commonly used surfaces - Honeycomb and Hole-pattern.

in the rotor.

Nowadays manufacturers use either a honeycomb or a hole-pattern surface to build the seals as shown in fig. 3.7:

Regarding the modeling of these components, CHILDS [33] developed an analysis to calculate direct and cross-coupled terms of incompressible flow using bulk-flow theory and a perturbation technique. This work has provided a general basis for seal analysis.

Bulk-flow theory has been introduced by HIRS [34]. This theory does not make use of information or model on:

1. fluctuations of local velocities of flow due to turbulence;

2. the shape of flow velocity profiles from which fluctuating components have been eliminated through averaging.

Only the bulk-flow relative to a surface and the corresponding shear stress are considered and correlated. That is, the variation of fluid velocity components across the clearance is neglected, and average (across the clearance) velocity components are used, hence, the bulk-flow designation (CHILDS [32]).

The theory is based on the empirical finding that the wall-shear stress and mean velocity of flow can be expressed as a relation with empirical numerical constants to be fitted to the available experimental results.

This relation between wall-shear stress and mean velocity of flow relative to the wall at which the shear stress is exerted can be expressed as

$$\tau = \frac{1}{2}\rho U_m^2 n_0 \left(\frac{2\rho U_m h}{\mu} \right)^{m_0} \tag{3.59}$$

where τ is the wall-shear stress, ρ is the fluid density, U_m is the mean flow velocity, h is the film thickness, n_0 and m_0 are empirical constants.

The empirical constants can be derived from bulk-flow measurements and do not require the determination of flow velocity profiles.

NELSON [35] derived governing equations for compressible flow in a tapered annular seal using the general basis developed by CHILDS [33], by applying the bulk-flow theory and a perturbation technique. This model was based on:

- a compressible-flow continuity equation;
- an axial-momentum equation;
- a circumferential-momentum equation;
- an energy equation;
- a perfect-gas equation of state.

In the NELSON [35] model the seal stator surface was treated as a solid wall with an increased friction factor in the momentum equations. No consideration was given to the cell geometry when defining the control volume.

This model did a poor job in predicting measured rotordynamic coefficients. Attempts to improve the model were made by ELROD *et al.* [36] and HA and CHILDS [37], but they also failed because of their assumption that the problem was related to their friction-factor model.

HA and CHILDS [14] showed that the friction-factor was dependent on cell geometry. In their work, the friction-factor has been measured for flat-plates with honeycomb surfaces. In some cases, contrary to a turbulent flow in a pipe where the friction factor decreases as the Reynolds number increases, the data showed

a 'friction-factor-jump'. HA *et al.* [38] demonstrated that this phenomenon is explained by acoustic excitation of a coherent flow structure which impact the main flow.

Following the discussion of the work from HA and CHILDS [37], SCHARRER [39] mentioned that the application of different friction models was somewhat futile and that similar attempts were made to model labyrinth seals. In the discussion it is mentioned that, in labyrinth seal analysis, significant progress could only be achieved after the application of a more realistic model by SCHARRER [40], where a two-control volume was used. Based on this discussion KLEYNHANS and CHILDS [41] carried out the implementation of a different model considering the following:

- a two-control-volume as shown in fig. 3.8;
- a compressible-flow continuity equation;
- an axial-momentum equation;
- a circumferential-momentum equation;
- isothermal flow - no energy equation required;
- a perfect-gas equation of state.

The governing equations are the following:

The continuity equation for the control volume A is given by

$$0 = \frac{\partial}{\partial t}(\rho H) + \frac{1}{R}\frac{\partial}{\partial \theta}(\rho U H) + \frac{\partial}{\partial Z}(\rho W H) + \rho V \tag{3.60}$$

where U is the circumferential bulk fluid velocity, W is the axial bulk fluid velocity, V is the radial bulk fluid velocity, H is the seal clearance and R is the radius.

For the control volume B we have

$$\rho V = H_d \frac{\partial \rho}{\partial t} \tag{3.61}$$

where H_d is the cell hole depth.

Notice that the addition of the second control volume that allows flow to only enter and exit in the radial direction (V) improves the model regarding the cell acoustic behavior. It is also important to notice that if there is no perturbation $V = 0$. This model leads to a strong frequency-dependent behavior of the seal's coefficients.

We can use eq. (3.61) in eq. (3.60) to eliminate V:

$$0 = \frac{\partial}{\partial t}(\rho(H + \gamma_c H_d)) + \frac{1}{R}\frac{\partial}{\partial \theta}(\rho U H) + \frac{\partial}{\partial Z}(\rho W H) \tag{3.62}$$

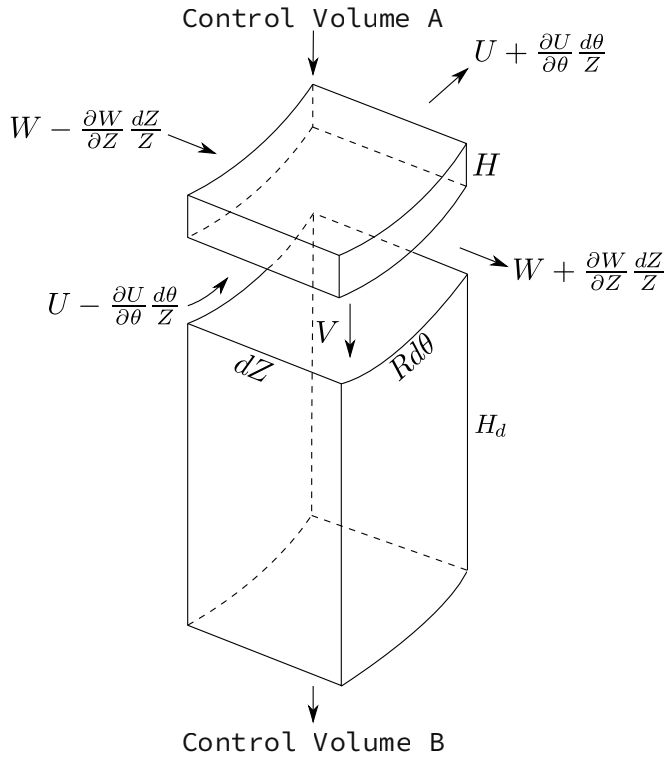

Figure 3.8: Control volume for a honeycomb seal stator KLEYNHANS [4].

where γ_c is the ratio between the area covered by cells and the seal total area. The product $\gamma_c H_d$ will be referred in this work as c - cell to volume area ratio.

The equation for the axial Momentum is

$$0 = \rho H \frac{\partial W}{\partial t} + \frac{\rho U H}{R}\frac{\partial W}{\partial \theta} + \rho W H \frac{\partial W}{\partial Z} + H\frac{\partial P}{\partial Z} + \tau_{sz} + \tau_{rz} \tag{3.63}$$

Considering the circumferential Momentum we get

$$0 = \rho H \frac{\partial U}{\partial t} + \frac{\rho U H}{R}\frac{\partial U}{\partial \theta} + \rho W H \frac{\partial U}{\partial Z} + \frac{H}{R}\frac{\partial P}{\partial Z} + \tau_{s\theta} + \tau_{r\theta} \tag{3.64}$$

where τ represents the shear component and the subscripts s and r mean stator and rotor respectively.

Finally, the state equation (ideal gas), which will be used to calculate ρ is written as:

$$P = \rho z_c R_g T \tag{3.65}$$

where P is the pressure, z_c is the compressibility factor, R_g is the gas constant and T is the temperature.

The boundary conditions to account for contraction and expansion at the seal

inlet and exit are

$$P_i - P(0) = \frac{1+\xi_i}{2}\rho(0)[W(0)^2] \tag{3.66}$$

$$P_e - P(L) = \frac{1+\xi_e}{2}\rho(L)[W(L)^2] \tag{3.67}$$

where ξ_i and ξ_e are the inlet loss and exit recovery factors.

At the inlet the flow direction is also specified:

$$u(0) = \Omega_w R\omega \tag{3.68}$$

As described in KLEYNHANS and CHILDS [41] the solution of the above equation follows a procedure that employs a perturbation of the variables P, H, W, U and ρ by the eccentricity ratio as $\phi(Z,\theta,t) = \phi_0(Z) + \epsilon\phi_1(Z,\theta,t)$, where ϕ are the primitive flow variables and ϵ is the eccentricity ratio.

The zeroth-order equations are solved for the steady-flow and leakage. The first-order equations are used to calculate the fluid reaction forces and rotordynamic coefficients.

The method developed by KLEYNHANS and CHILDS [41] will be used in the current work. This method has been implemented in the Texas A&M software ISOTSEAL. As shown in eq. (3.59), the bulk-flow theory requires a method to evaluate the friction factors for the rotor and stator considering the empirical coefficients n_0 and m_0.

Lacking experimental data an estimation method can be used, such as Colebrook's formula NELSON [42]. MIGLIORINI *et al.* [43] proposes a hybrid method where CFD is applied to solve the base state flow, and a bulk-flow perturbation method is used to solve for the fluid forces acting on an eccentric, whirling rotor. In the current work, friction factors given by MIGLIORINI *et al.* [5] for a similar seal will be used.

3.5 Deterministic Model

The general form of the equation for the system, after matrix assembly is (FRISWELL [2])

$$\mathbf{M}\ddot{\mathbf{q}} + \mathbf{C}(\mathbf{\Omega})\dot{\mathbf{q}} + \Omega\mathbf{G}\dot{\mathbf{q}} + \mathbf{K}(\mathbf{\Omega})\mathbf{q} = \mathbf{f} \tag{3.69}$$

where $\mathbf{q}$ represents the displacements and rotations at the nodes, $\mathbf{M}$, $\mathbf{K}$, $\mathbf{C}$ and $\mathbf{G}$ are the mass, stiffness, damping and gyroscopic matrices, and $\mathbf{f}$ is the generalized force vector.

In an example with 3 elements, the model will have 4 nodes. Each node will have 4 degrees of freedom, resulting in a global matrix of 16x16. The first element

contains degrees of freedom 1 to 8, the second element the degrees of freedom 5 to 12, and the third element the degrees of freedom 9 to 16. The coefficients for each shaft, disk, bearing and seal elements are placed at the corresponding degree of freedom to assemble the global matrices.

Writing eq. (3.69) using the state vector $(\mathbf{q}, \dot{\mathbf{q}})$, for free-vibration, we have:

$$\frac{d}{dt}\begin{bmatrix}\mathbf{q}\\ \dot{\mathbf{q}}\end{bmatrix} = \begin{bmatrix}\mathbf{0} & \mathbf{I}\\ -\mathbf{M^{-1}K} & -\mathbf{M^{-1}}(\mathbf{C}+\omega\mathbf{G})\end{bmatrix}\begin{bmatrix}\mathbf{q}\\ \dot{\mathbf{q}}\end{bmatrix} \tag{3.70}$$

where the dependence of the stiffness and damping matrices on the excitation frequency Ω is omitted.

If $\mathbf{x} = (\mathbf{q}, \dot{\mathbf{q}})$, we compact eq. (3.69)

$$\dot{\mathbf{x}}(t) = \mathbf{A}\mathbf{x}(t) \tag{3.71}$$

with solutions of the form

$$\mathbf{x}(t) = \mathbf{v}e^{st} \tag{3.72}$$

Substituting eq. (3.72) in eq. (3.71):

$$\mathbf{A}\mathbf{v} = \lambda\mathbf{v} \tag{3.73}$$

Equation (3.73) is a generalized eigenvalue problem with 2n solutions of the form

$$s_i, s_{n+i} = \omega_i\Big(-\zeta_i \pm \sqrt{1-\zeta_i^2}\Big) = -\zeta_i\omega_i \pm j\omega_{di} \tag{3.74}$$

where ω_i and ζ_i are the i-th natural frequency and the i-th damping ratio that are used to evaluate the rotor stability.

The forced response, in the frequency domain, can be calculated by

$$\mathbf{q}(\omega) = [-\omega^2\mathbf{M} + j\omega(\omega\mathbf{G}+\mathbf{C}) + \mathbf{K}]^{-1}\mathbf{f}(\omega) \tag{3.75}$$

where $\alpha = [-\omega^2\mathbf{M} + j\omega(\omega\mathbf{G}+\mathbf{C}) + \mathbf{K}]^{-1}$ is the receptance matrix.

3.6 Stochastic Model

For a compressor operating with a suction pressure of 250 bar, damper seal coefficients have been calculated using ISOTSEAL, which is a private software produced by Texas A&M and is based on a bulk-flow and Blasius friction factor model (KLEYNHANS [4]). The values calculated are shown in fig. 3.9.

The compressor's vendor proposed a correction to the values calculated based

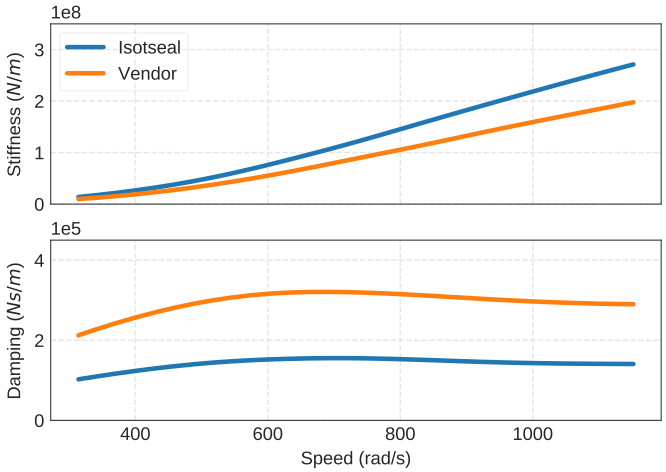

Figure 3.9: Seal coefficients calculated with ISOTSEAL and by the vendor.

on internal experiments done on a seal test rig. These tests were not carried out at the compressor operational conditions and the correction applied can be considered as an extrapolation of experimental results. These coefficients will be identified in the current work as 'Vendor's coefficients'.

As shown in fig. 3.9, the coefficients values proposed by the vendor differ from those obtained using ISOTSEAL. Actually, for the operational conditions of interest, it is not easy to accurately determine the seal coefficients. In this work synchronous coefficients will be used, e.g. $K_{xx}(\Omega)$, where Ω is the rotor precession that in our case is equal to the nominal rotation of the machine.

Let $a(\Omega)$ represent a seal coefficient (K_{xx}, $, k_{xy}$, etc). We will model it as a stochastic process $\{A(\Omega) : \Omega \in W\}$ (frequency indexed), which is a collection of random variables defined on a common probability space. First, let us define the deterministic functions. The two curves shown in fig. 3.9 are used as references for our seal coefficients model: (1) the result obtained by a bulk-flow model (ISOTSEAL) and (2) the results available by the vendor. The following function, which considers a linear interpolation between the two curves, is then applied

$$a(\Omega) = (1 - f)a_1(\Omega) + f a_2(\Omega) \tag{3.76}$$

where $a_1(\Omega)$ is the coefficient curve obtained by the bulk- flow model (ISOTSEAL) and $a_2(\Omega)$ by the vendor's values and f is an interpolation factor.

When the correction factor equals to one, we have the vendor's curve, and when $f = 0$, we have the bulk-flow model result. Therefore, the resulting coefficient $a(\Omega)$ is a mixing of the two models. If $0 < f < 1$ we get a curve between these two cases; this is illustrated in fig. 3.10, where curves with $f = 0.3$ and $f = 0.7$ are plotted. Note that depending on the coefficient $a_1 > a_2$ or $a_2 > a_1$.

The proposed stochastic model considers the interpolation factor f a random

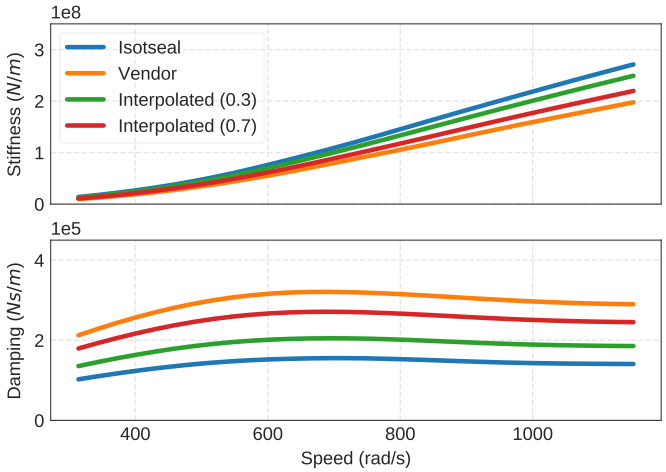

Figure 3.10: Example of random interpolation factors applied to obtain an interpolated curve.

variable F, so that the random process is given by

$$A(\Omega) = (1 - F)a_1(\Omega) + Fa_2(\Omega) \tag{3.77}$$

This means that the proposed uncertain model for the seal coefficients considers that each observation of the stochastic process has a shape similar to the curves shown in fig. 3.9, and each observation is shifted up or down on fig. 3.10.

If (i) the support of F is bounded, $[F_{min}, F_{max}]$, (ii) the mean value is $E\{F\} = (F_{min}+F_{max})/2$, and (iii) no other information is known (for instance, knowlegdment of other statistical moments), the maximum entropy principle (JAYNES [44]) yields a Uniform distribution for F. Thus, the probability density function is given by $p_F = 1/(F_{max} - F_{min})$ within the bounds. Hence $A(\Omega)$ is a Uniform stochastic process, i.e., for a fixed Ω, $A(\Omega)$ follows a Uniform distribution.

Since the coefficients are random, the response of the system, observed in the Campbell diagram, and in the rotor unbalance response, is also random. The stochastic system is then

$$\mathbf{M}\ddot{\mathbf{Q}} + \mathcal{C}(\Omega)\dot{\mathbf{Q}} + \Omega\mathbf{G}\dot{\mathbf{Q}} + \mathcal{K}(\Omega)\mathbf{Q} = \mathbf{f} \tag{3.78}$$

where the damping and stiffness random matrices $\mathcal{C}(\Omega)$ and $\mathcal{K}(\Omega)$ are random because of the random damper seal coefficients. Thus the response is also random $\mathbf{Q}$.

3.7 Robust Optimization

Provided that the general system design has been fixed, the optimization process can be described as choosing the right design parameters $\mathbf{x}$ according to an (or some) objective function(s) $f(\mathbf{x})$. Typically, design constraints are also imposed on $\mathbf{x}$. This problem has the form (BOYD and VANDENBERGHE [45]):

$$\begin{array}{ll} \text{minimize} & f_0(\mathbf{x}) \\ \text{subject to} & f_i(\mathbf{x}) \leq b_i, i = 1, ..., m. \end{array} \tag{3.79}$$

The vector $\mathbf{x} = (x_1, \ldots, x_n)$ is the optimization variable, the function $f_0 : \mathbf{R}^n \rightarrow \mathbf{R}$ is the objective function, the functions $f_i : \mathbf{R}^n \rightarrow \mathbf{R}, i = 1, \ldots, m$, are the constraint functions, and the constraints $b_1, \ldots, b_m$ are the limits for the constraints. A vector $\mathbf{x}^*$ that has the smallest objective value and satisfy the constraints is called optimal.

BEYER and SENDHOFF [46] provides some questions about whether it is desirable to locate isolated, singular design points:

1. Objective and constraint functions always represent models of the real world. As long as one does not have detailed knowledge of the error function of the model, one cannot be certain the model optimum can be mapped to the true optimum;

2. Even if we are able to map the model optimum, one might not be able to build the true optimum due to manufacturing uncertainties or manufacturing cost;

3. The formulation of the optimization problem in eq. (3.79) is static. Reality is dynamic: environmental parameters fluctuate, materials wear down, parts of the system might be replaced.

Systems optimized in the classical sense can be very sensitive to small changes.

Robust design can be used to minimize the effect of the causes of variation without eliminating these causes, as described by ZANG *et al.* [47]. The objective is to optimize the mean performance and minimize its variation. Optimization of the mean often conflicts with minimizing the variance, and a trade-off decision between them is needed to choose the best design.

In the field of rotordynamics, RITTO *et al.* [48] has proposed a methodology to optimize the performance of a flexible rotor-bearing system taking into account uncertainties in parameters such as the stiffness of the bearing and the elasticity modulus of the material.

ZANG *et al.* [47] shows the application of robust optimization to design a vibration absorber with mass and stiffness uncertainty. In the present work, a similar approach will be used.

Three specific objective functions will be used. They are defined as follows:

- $f_1(L, c)$ evaluates the vibration amplitude at the Non-Drive-End side (NDE) probe (sensor located at node 50) at operating speed;
- $f_2(L, c)$ evaluates the lowest logarithmic decrement between the first and second forward mode at operating speed. These modes are chosen due to the fact that they are the closest to the operating speed and the forward mode is the one that will become unstable with a high cross-coupled stiffness;
- $f_3(L, c)$ evaluates the mass leakage for the seal at operating speed. The leakage is directly calculated by ISOTSEAL.

where the design parameters are L and c, which are respectively the seal length and the cell volume to area ratio. The parameter c is calculated as:

$$c = \gamma H_D \tag{3.80}$$

where H_D is the mean cell depth and γ is the seal area covered by cells and the total seal area. This value is normally close to 0.8 for honeycomb and hole-pattern seals.

These objective functions are combined into a single objective function and the deterministic optimization problem is

$$\begin{array}{ll} \text{minimize} & [\sum_{i=1}^{3} \beta_i f_i(L, c)] \\ \text{subject to} & 65 \leq L \leq 95, \quad 1.5 \leq c \leq 3.5 \end{array} \tag{3.81}$$

The factors β_i are weights given to each function and they are chosen with the following constraints:

$$\beta_i < 1, \forall i \in \{1, 2, 3\} \tag{3.82}$$

$$\sum_{i=1}^{3} \beta_i = 1 \tag{3.83}$$

To construct the robust optimization problem we have to consider not only the deterministic value from each function f_i, but also its variance when we apply the stochastic model proposed in section 3.6. Each specific objective function will be of the form $f_i(\mu_i, {\sigma^2}_i, \alpha_i)$ where μ_i is the mean ${\sigma^2}_i$ is the variance and $\alpha_i \in [0, 1]$ is a weighting factor that represents the relative importance between the mean and the variance.

To combine the mean and the variance into a single objective function, we define an utopia design point $[\mu_i^U, {\sigma^2}_i^U]$, calculated by minimization of μ_i and ${\sigma^2}_i$ individually as single objective functions and the nadir point $[\mu_i^N, {\sigma^2}_i^N]$ which is calculated by maximizing μ_i and ${\sigma^2}_i$ also individually.

The robust objective function f is then written

$$f_i(\mu_i, {\sigma^2}_i, \alpha_i) = \alpha_i \frac{\mu_i(L,c) - \mu_i^U}{\mu_i^N - \mu_i^U} + (1-\alpha_i)\frac{{\sigma^2}_i(L,c) - {\sigma^2}_i^U}{{\sigma^2}_i^N - {\sigma^2}_i^U} \tag{3.84}$$

And the robust optimization problem can be written as:

$$\begin{array}{ll} \text{minimize} & [\sum_{i=1}^{3} \beta_i f_i(\mu_i, {\sigma^2}_i, \alpha_i)] \\ \text{subject to} & 65 \leq L \leq 95, \quad 1.5 \leq c \leq 3.5 \end{array} \tag{3.85}$$

It is important to notice here that in our problem the design parameters L and c, which represents the seal's length and cell volume to area ratio are not random, but the $\mathcal{C}(\Omega)$ and $\mathcal{K}(\Omega)$ matrices are random, as defined by the stochastic model presented in section 3.6.

The procedure for the robust optimization here can be summarized as follows:

1. Determine nadir and utopia by optimizing functions individually;
2. Choose initial value for L and c;
3. Calculate the deterministic matrices $\mathbf{K}(\Omega)$ and $\mathbf{C}(\Omega)$ given a value for L and c using the method presented by KLEYNHANS and CHILDS [41] (with ISOTSEAL software), considering the synchronous coefficients;
4. Calculate the deterministic 'vendor' matrices $\mathbf{K}(\Omega)$ and $\mathbf{C}(\Omega)$ considering that the vendor $\mathbf{K}$ is 70% from the value calculated with ISOTSEAL and the vendor $\mathbf{C}$ is 200% from the value calculated with ISOTSEAL. The values of 70% for the stiffness and 200% for the damping were obtained by analyzing the extrapolation given by the vendor and described in section 3.6;
5. Apply the stochastic model presented in section 3.6 to obtain the random matrices $\mathcal{C}(\Omega)$ and $\mathcal{K}(\Omega)$;
6. Use Monte Carlo simulations to calculate the mean and variance;
7. Calculate the objective according to eq. (3.84) and eq. (3.85);

These steps can then be used with a suitable optimization algorithm to find the optimal solution.

Chapter 4

Results

4.1 Deterministic Model Results

To evaluate the compressor rotordynamic behavior a finite element model written in python considering the mathematical modeling described in chapter 3 is used. The codes were developed using libraries numpy (WALT *et al.* [49]), scipy (JONES *et al.* [50]) and matplotlib (HUNTER [51]).

Figure 4.1 displays the rotor system that will be analyzed in this work. Parts in orange represent lumped masses at the impeller and coupling locations. Bearings are represented as blue triangles. The shaft elements are in gray. A second layer (lighter gray) with elements that have no stiffness or damping was used to represent the dry gas seals parts.

Shaft elements have the following properties:

- Density: $7833.41\,\mathrm{N/m^3}$;
- Young's modulus $2.068 \times 10^{-11}\,\mathrm{N/m^2}$;
- Shear modulus $8.273 \times 10^{-10}\,\mathrm{N/m^2}$.

Dimension and position for each shaft and disk element are given in the appendix.

The coefficients for the bearings were obtained from MAXBRG software (HE [28]) and are presented in fig. 4.2 and fig. 4.3. Figure 4.2b shows low cross-coupled coefficients when compared to damping coefficients. This is expected since tilting-pad bearings with cylindrical pivot arrangement were used.

To validate the code used in this work, the same model has been constructed using the XLTRC2 software (from Texas A&M Turbomachinery CONSORTIUM [52]).

Figure 4.4 shows the undamped critical speed map calculated using the developed code and the XLTRC2 software. This map is generated by varying the support

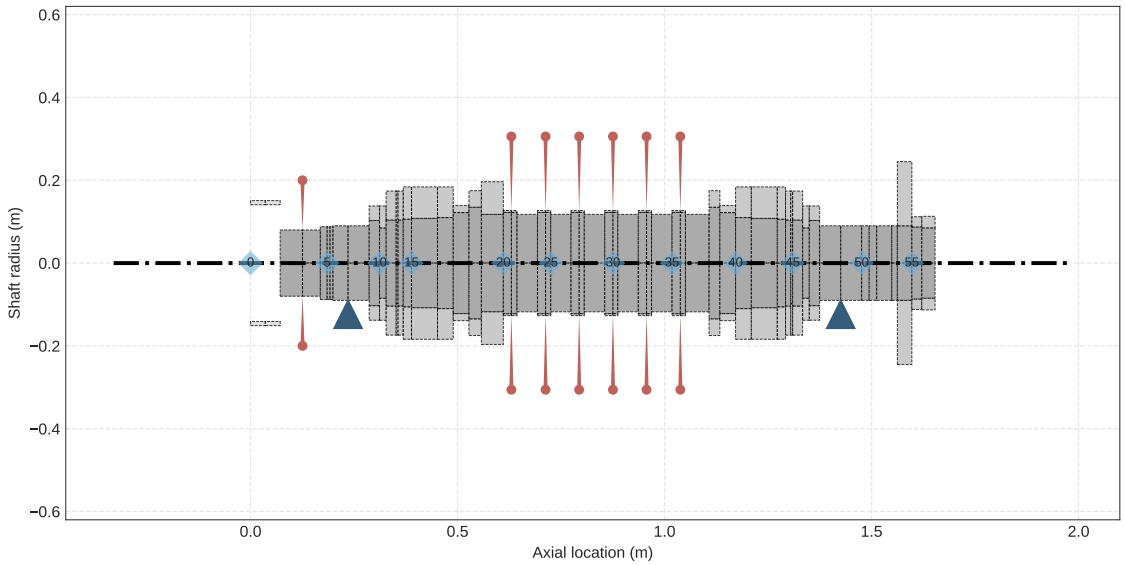

Figure 4.1: Rotor model.

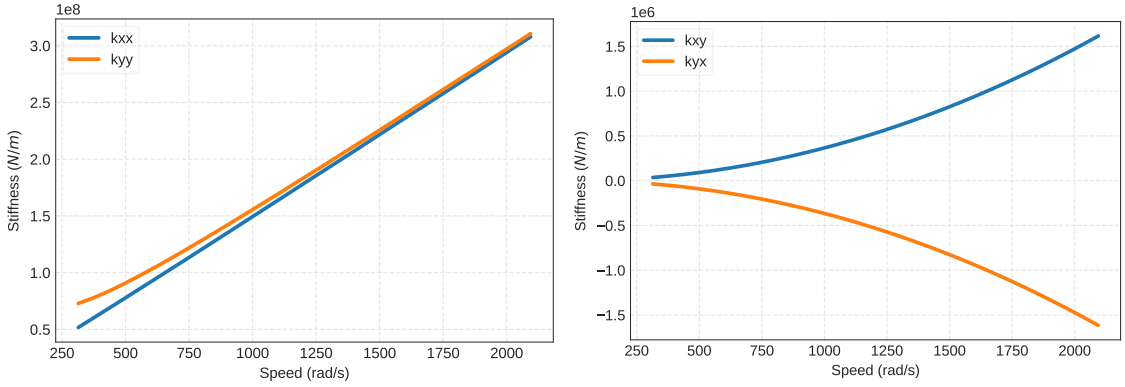

(a) Direct coefficients.

(b) Cross coupled coefficients.

Figure 4.2: Bearing stiffness coefficients.

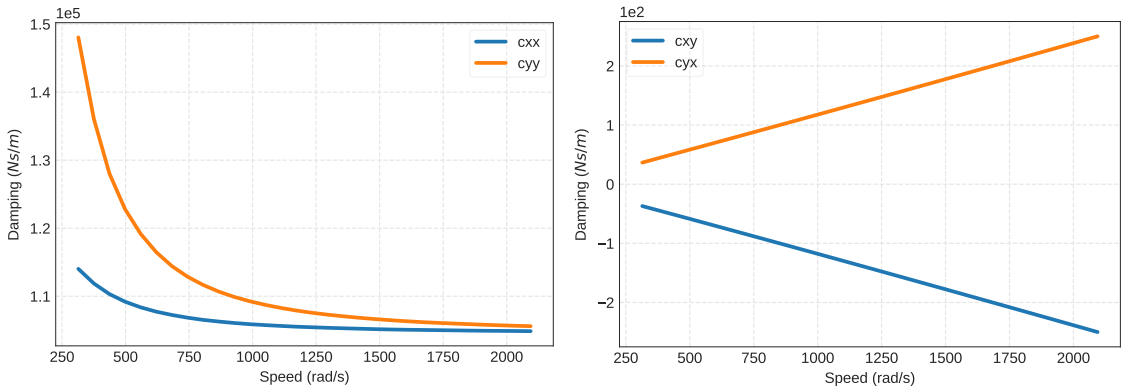

(a) Direct coefficients.

(b) Cross coupled coefficients.

Figure 4.3: Bearing damping coefficients.

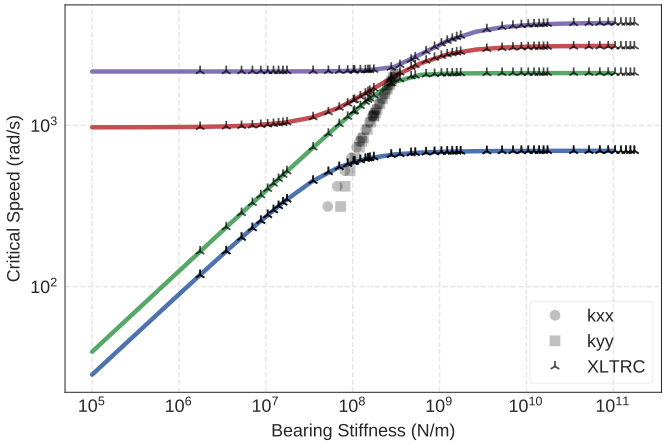

Figure 4.4: Undamped critical speed map.

stiffness in a given range and calculating the natural frequencies for the rotor. The rotor speed in this case is considered to be zero. The good agreement between results shows that the developed code for the shaft model (with Timoshenko beam elements) is presenting consistent results for all evaluated modes.

To evaluate the gyroscopic effect on the natural frequencies, it is useful to use the natural frequency map (also known as Campbel diagram). Before evaluating these results we discuss how the gyroscopic effects on a rigid rotor on isotropic supports without damping. For this case the equations of motion are defined by FRISWELL [2] as:

$$\begin{aligned} m\ddot{u} + k_T u + k_C \psi &= 0 \\ m\ddot{v} + k_T v - k_C \theta &= 0 \\ I_d\ddot{\theta} + I_p\omega\dot{\psi} - k_C v + k_R\theta &= 0 \\ I_d\ddot{\psi} - I_p\omega\dot{\theta} + k_C u + k_R\psi &= 0 \end{aligned} \tag{4.1}$$

where u and v represent translation along Ox and Oy axes and θ and ψ represent clockwise rotations about axes Ox and Oy as presented in fig. 3.3. The moment of inertia about the longitudinal axis is I_p and the moment of inertia with respect to the diameter of the rotor is I_d. The rotor speed is ω and the subscripts T, C and R indicate translational, coupling between displacement and rotation, and stiffness coefficients.

As isotropic supports were considered, $k_C = 0$, the first two equations uncouple to give:

$$\omega_1 = \omega_2 = \sqrt{\frac{k_T}{m}} \tag{4.2}$$

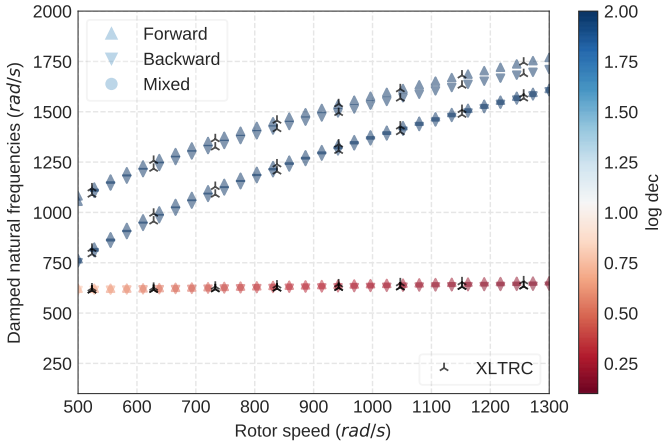

Figure 4.5: Campbell diagram.

After some algebraic steps the second pair of equation can be solved to give:

$$\omega_3 = -\frac{I_p\omega}{2I_d} + \sqrt{\left(\frac{I_p\omega}{2I_d}\right) + \frac{k_R}{I_d}} \tag{4.3}$$

$$\omega_4 = \frac{I_p\omega}{2I_d} + \sqrt{\left(\frac{I_p\omega}{2I_d}\right)^2 + \frac{k_R}{I_d}} \tag{4.4}$$

These natural frequencies are dependent of rotation. Depending on the relation between angles θ and ψ the mode direction of rotation will be *forward*, if in the same direction of the rotor speed, or *backward* if in the opposite direction. In the developed code this direction is evaluated for each node of the rotor, in this case we can also have a *mixed* mode, in which some nodes have a forward precession and some have a backward precession.

Figure 4.5 shows the Campbell diagram. The plot has been generated by varying the rotor speed and calculating the corresponding natural frequencies and evaluating the nodes at each mode shape to determine if they have forward or backward precession. There is a good agreement between results, showing that gyroscopic effects and the bearings coefficients are correctly handled by the developed code. Notice that results below 500 rad/s were omitted since the calculated bearing coefficients are not reliable in this speed range.

To carry a level 1 stability analysis a cross coupling Q_a, varying from 0 to $3\,500\,000\,\mathrm{N\,m^{-1}}$, is inserted in the middle of the rotor (node 29), as shown in fig. 4.6 and the log decrement for the first forward mode is evaluated.

Figure 4.7 shows the level 1 stability analysis results. A good agreement was also obtained in this case, showing that the calculated log decrement for an inserted cross coupling is consistent for the used code.

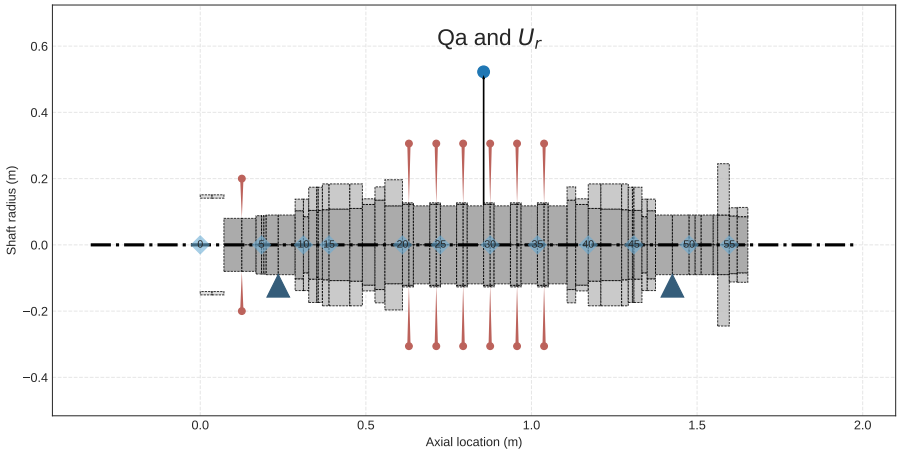

Figure 4.6: Campbell diagram.

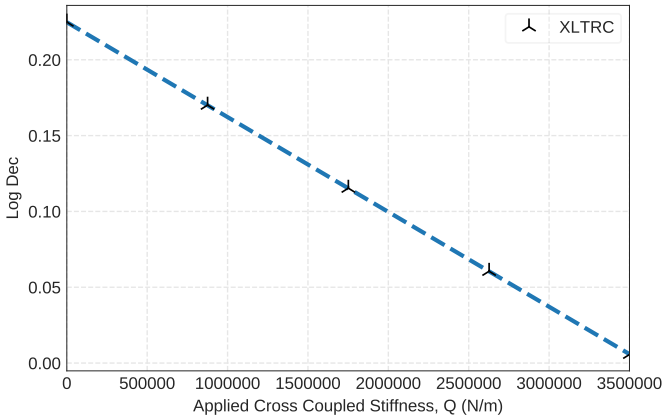

Figure 4.7: Level 1 stability analysis.

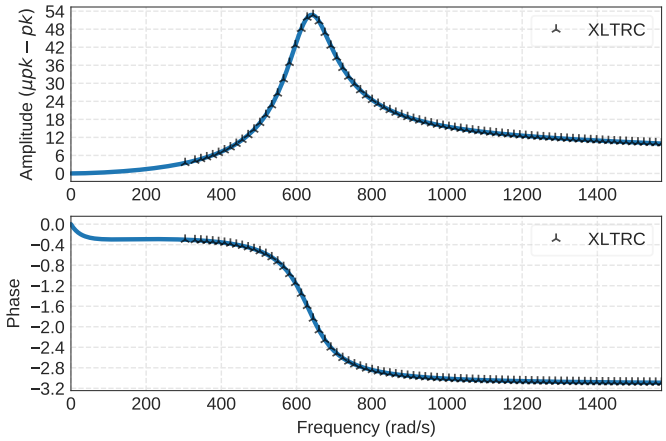

Figure 4.8: Unbalance response.

Figure 4.8 shows the response to an unbalance placed in the middle of the rotor (node 29), also presenting a good agreement between results.

4.2 Stochastic Results

The Campbell diagram for the condition without the seal is presented in fig. 4.9a. For each rotor speed (x axis) the eigenvalues are calculated from eq. (3.74) and the frequency of oscillation for the damped system are plotted (y axis). We can see that around 600 rad/s the system crosses a critical speed. The eigenvalues also provide information regarding the damping factor, which is used to calculate the log dec for each natural frequency. This information is presented in the marker color. Different markers are used to show which modes have a forward precession (same orientation as the shaft rotation), a backward mode or a mixed mode.

To give an idea of how the Campbell diagram is affected by the damper seal

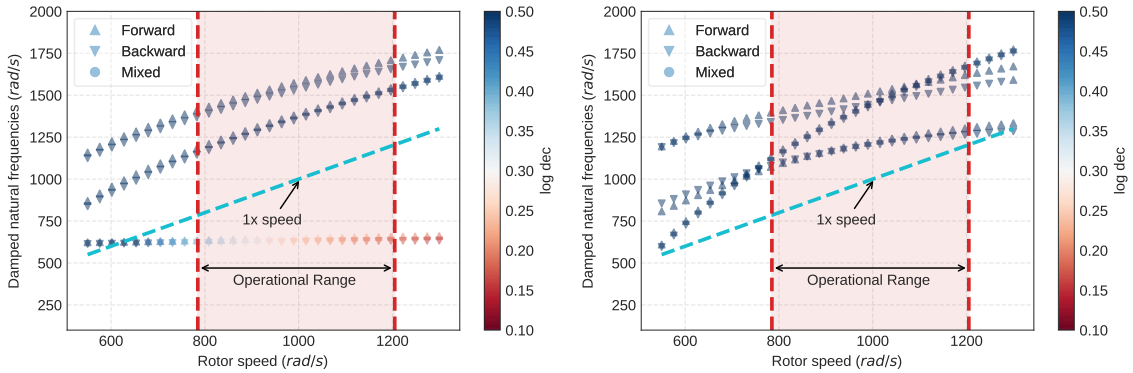

(a) Without the damper seal.

(b) With damper seal.

Figure 4.9: Campbell constructed with and without considering the damper seal. The campbell with damper seal uses the ISOTSEAL coefficients.

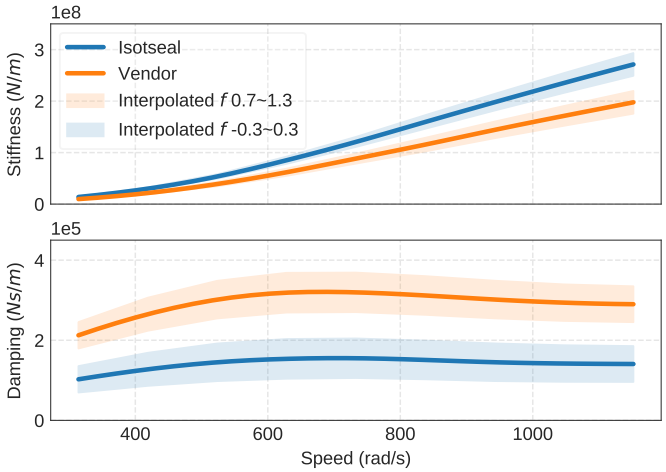

Figure 4.10: Two different f intervals that will be analyzed.

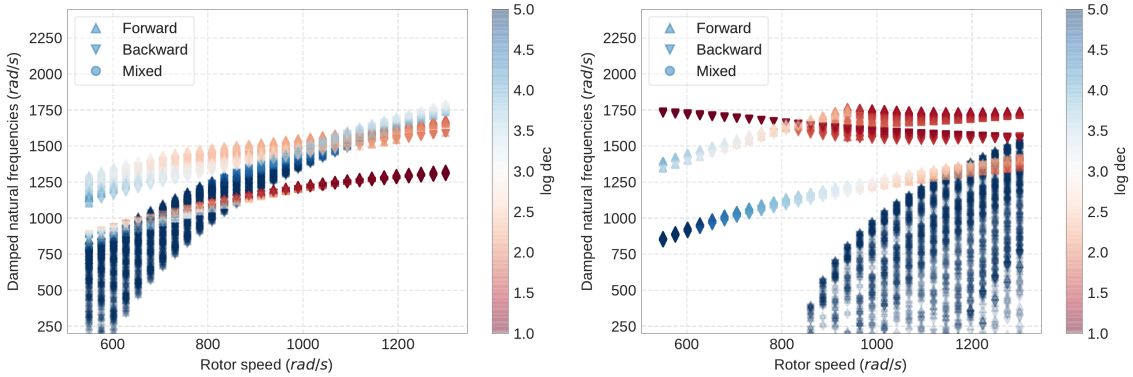

(a) Interpolation interval around the ISOTSEAL coefficients.

(b) Interpolation interval around the vendor coefficients.

Figure 4.11: Campbell considering different interpolation intervals.

coefficients, fig. 4.9b shows the analysis considering the ISOTSEAL coefficients. From the six modes shown, we can note that the first two modes shift upward, and the intersection between the synchronous speed (1 × nominal rotor speed) occurs inside the operational range. Other modes are also affected and fig. 4.9b shows that the damper seal increases the log dec especially for the first two modes.

Two different intervals will also be analyzed to help the understanding of how the coefficients affect the diagram. These intervals are shown in fig. 4.10. To approximate the statistics of the response, the Monte Carlo method is employed.

For the first case (interpolation around the ISOTSEAL coefficients) the Campbell diagram is presented in fig. 4.11a. Notice that in this plot the log dec bar scale has been changed, since these values are much higher when we include the damper seal.

For the second case (interpolation around the vendor coefficients) the Campbell diagram is presented in fig. 4.11b.

An analysis considering a wide interval of the interpolation factor, from -0.1 to

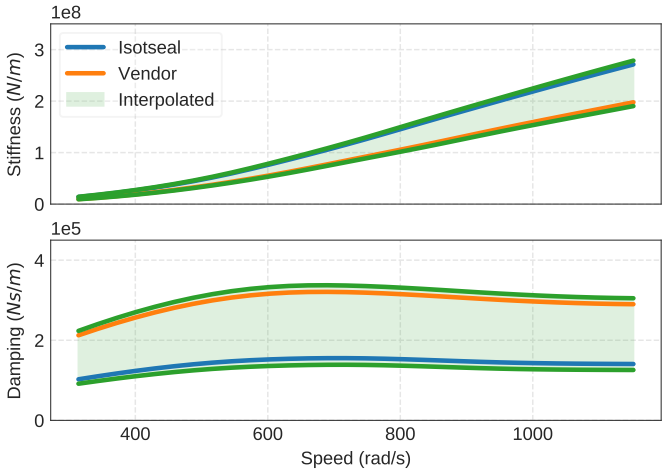

Figure 4.12: Coefficients interval that will be analyzed.

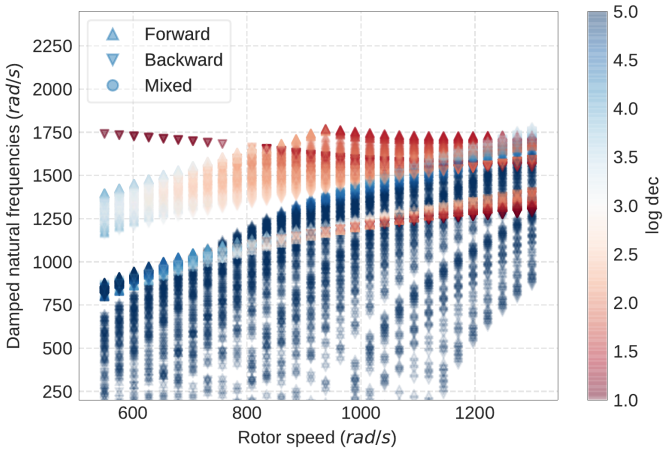

Figure 4.13: Campbell random curves obtained from an interval with interpolation factors F of -0.1 and 1.1.

1.1, is also be evaluated. This gives us an idea of how the uncertainties impact the Campbell diagram and the unbalance response. Figure 4.13 shows the Campbell diagram for random curves obtained from an interval with interpolation factors F of -0.1 and 1.1.

Some conclusions can be drawn:

1. The seal affects considerably the system response (see fig. 4.9a and fig. 4.9b)

2. The values of the log decrement are much higher when the seal is included in the analysis (being above 0.8 in all cases when API limit is 0.1)

3. Figure 4.9b shows that the natural frequency is increasing with the synchronous speed. This kind of behavior was also reported by BALDASSARRE *et al.* [24]

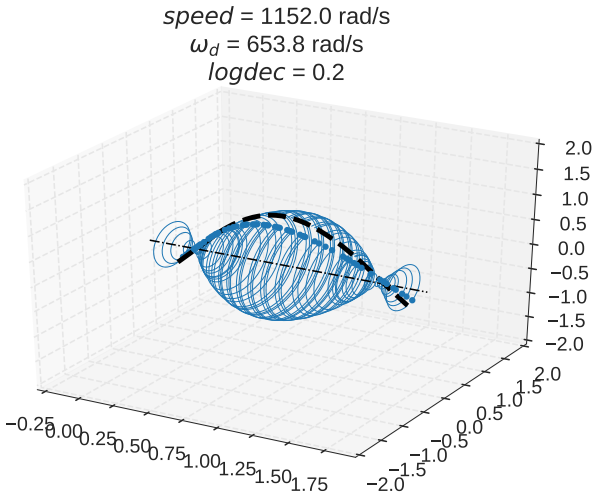

Figure 4.14: Mode shape for the first forward mode at 1200 rad/s on no seal condition.

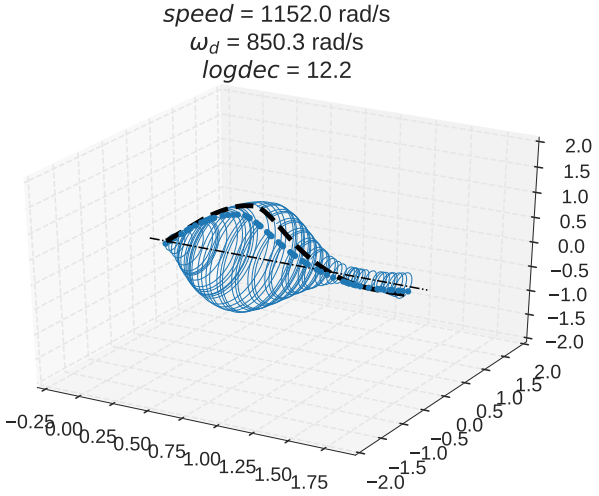

Figure 4.15: Mode shape for the first forward mode at 1200 rad/s with a factor f of 1.

4. Figure 4.9b shows that there is a natural frequency close to the maximum operating speed.

5. The system first natural frequency curve is very sensitive to uncertainties in the seal coefficients (see fig. 4.11a and fig. 4.11b).

6. The uncertainty in the response is very high if $F \in [-0.1, 1.1]$; see fig. 4.13.

Before evaluating the unbalance response the mode shape for the first forward mode is presented for comparison. Figure 4.14 shows the mode shape for the no seal condition and fig. 4.15 for a rotor with interpolation factor f equal to 1.

To verify the unbalance response two cases were evaluated. The first case considers an unbalance mass placed at the middle of the rotor (node 29) corresponding

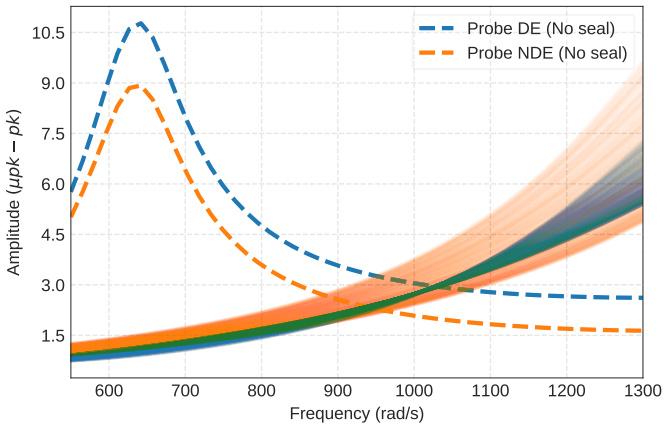

Figure 4.16: Rotor unbalance response at middle. Continuous lines are selected samples from the Monte Carlo simulation.

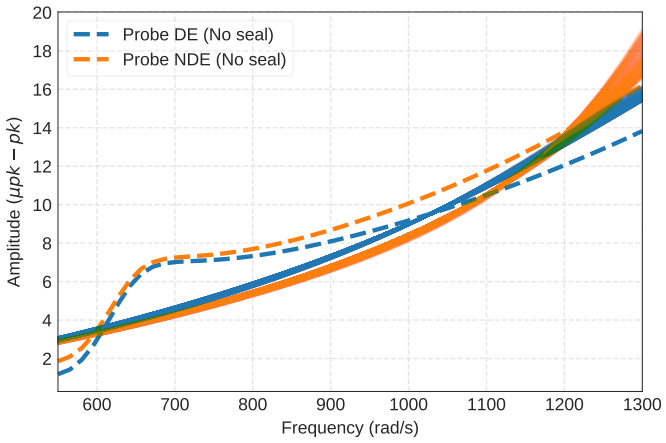

Figure 4.17: Rotor unbalance response at rotor end. Continuous lines are selected samples from the Monte Carlo simulation.

to 4 times the maximum residual unbalance determined by API 617 [1] (550 g.mm in this case). The second case distributes this unbalance between the rotor ends (nodes 0 and 57). All the unbalance masses have been placed considering a 0 phase angle and the vibration amplitude has been observed at the probe locations at the Drive-End side (DE), located at node 7, and at the Non-Drive-End side (NDE), located at node 50.

Figure 4.16 and fig. 4.17 show the response considering a no seal condition and the response obtained from the Monte Carlo simulation. The mean for the amplitude at the NDE (Non Drive End) probe at maximum speed was calculated at each simulation step and convergence was obtained when reaching around 400 iterations.

From the unbalance response results, we can conclude that:

1. The seal had a noticeable impact on the rotor unbalance response.

2. The response peak around 650 rad/s, in the no seal case, is not noticed in the case where the seal is present.

3. For the unbalance placed at the middle, the response close to the operating speed has increased 3 to 4 times when compared with the no seal case.

4. The standard deviation for the unbalance mass placed at the middle is also higher, especially in the NDE probe.

4.3 Robust Optimization

To evaluate the optimization the chosen interval for the seal length and cell volume to area ratio will be used to create a surface with the values of $h(L, c)$:

$$h(L, c) = \sum_{i=1}^{3} \beta_i f_i(\mu_i, \sigma^2{}_i, \alpha_i) \tag{4.5}$$

in which μ_i and $\sigma^2{}_i$ are dependent of L and c.

The specific objective functions that will be used are listed here again for clarity:

- $f_1(L, c)$ evaluates the vibration amplitude at the non-drive-end side probe at operating speed;

- $f_2(L, c)$ evaluates the lowest logarithmic decrement between the first and second forward mode at operating speed. These modes are chosen due to the fact that they are the closest to the operating speed and the forward mode is the one that will become unstable with a high cross-coupled stiffness;

- $f_3(L, c)$ evaluates the mass leakage for the seal at operating speed. The leakage is directly calculated by ISOTSEAL.

Two cases are presented. The first case considers the following:

$$\begin{aligned} \alpha_1 &= 0.8 \\ \alpha_2 &= 0.8 \\ \alpha_3 &= 1 \\ \beta_1 &= 0.6 \\ \beta_2 &= 0.35 \\ \beta_3 &= 0.05 \end{aligned} \tag{4.6}$$

The value of α_i close to 1 indicates that, for this case, the mean value has more importance than the variance. The value for α_3 is equal to 1 due to the fact that for the leakage we are going to consider only the mean value, since the leakage is not

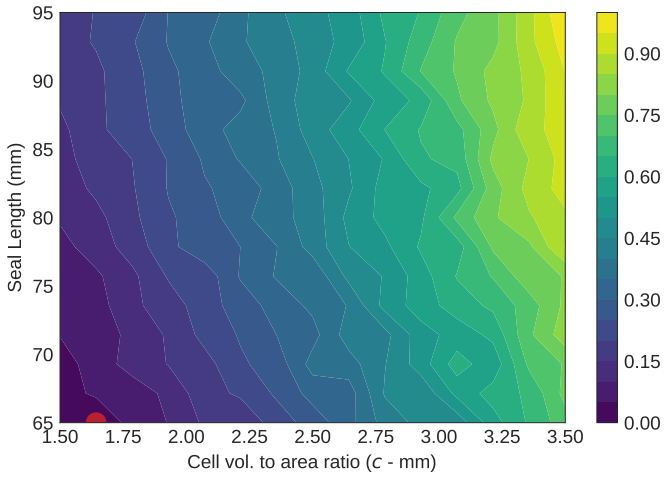

Figure 4.18: Optimization surface with $\alpha_1 = 0.8$, $\alpha_2 = 0.8$, $\alpha_3 = 1$ $\beta_1 = 0.6$, $\beta_2 = 0.35$ and $\beta_1 = 0.05$. Optimal point is shown by the red dot.

affected by the random matrices $\mathcal{C}(\Omega)$ and $\mathcal{K}(\Omega)$. The values for β are in decreasing order of importance, from the vibration amplitude at operating speed to the log dec and then to the seal leakage.

Results for this case are shown in fig. 4.18. The optimum point is the minimum value for seal length (65 mm) and is close to the minimum value for cell volume to area ratio (1.64 mm).

The second case considers the following:

$$\begin{aligned} \alpha_1 &= 0.2 \\ \alpha_2 &= 0.2 \\ \alpha_3 &= 1 \\ \beta_1 &= 0.6 \\ \beta_2 &= 0.35 \\ \beta_3 &= 0.05 \end{aligned} \tag{4.7}$$

In this case values for β are kept the same as in the previous case. The value of α_i in this case is close to 0 and the variance has a higher impact in the values of $h(L, c)$.

Figure 4.19 shows that in this case the optimum point is displaced to a seal length of 95 mm and a cell volume to area ratio of 1.5 mm.

To have a better understanding of the results shown in fig. 4.18 and fig. 4.19, each specific objective function will be evaluated separately regarding the impact of the seal length and cell volume to area ratio in the mean value and variance.

The first function evaluated is the probe-nde amplitude at operating speed - f_1. Figure 4.20 shows the results for this specific function.

To better understand the results we can evaluate the stochastic analysis for the

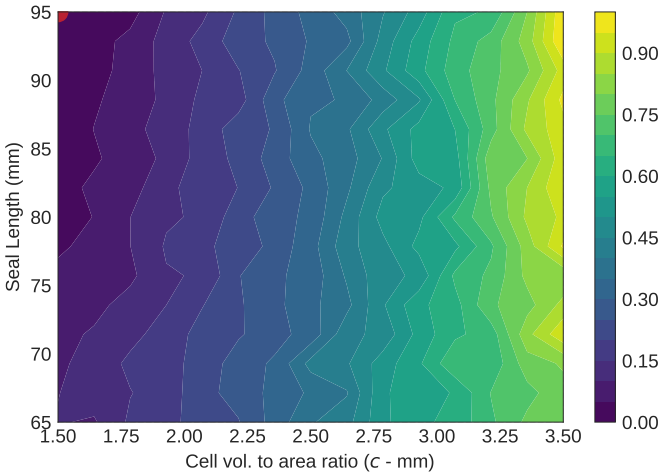

Figure 4.19: Optimization surface with $\alpha_1 = 0.2$, $\alpha_2 = 0.2$, $\alpha_3 = 1$, $\beta_1 = 0.6$, $\beta_2 = 0.35$ and $\beta_1 = 0.05$. Optimal point is shown by the red dot.

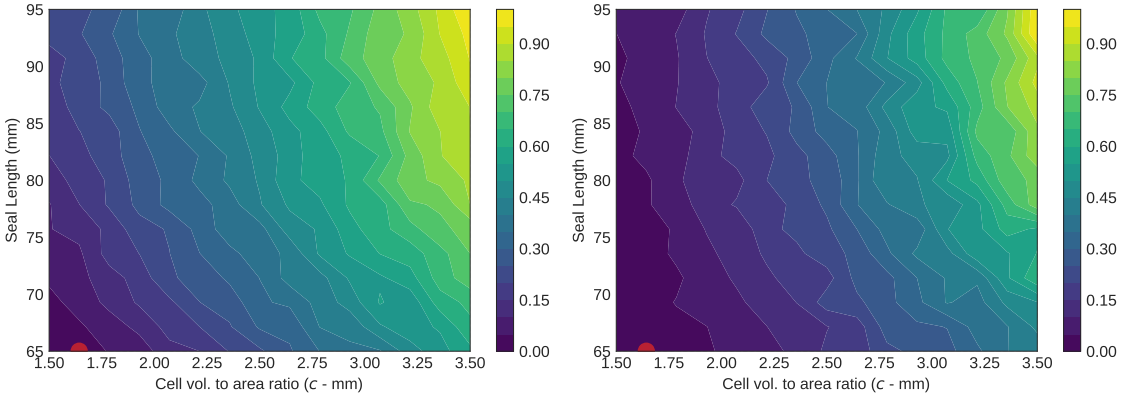

(a) f_1 mean - μ_1.

(b) f_1 variance - ${\sigma^2}_1$.

Figure 4.20: Surfaces for objective f_1 - amplitude at the operating speed.

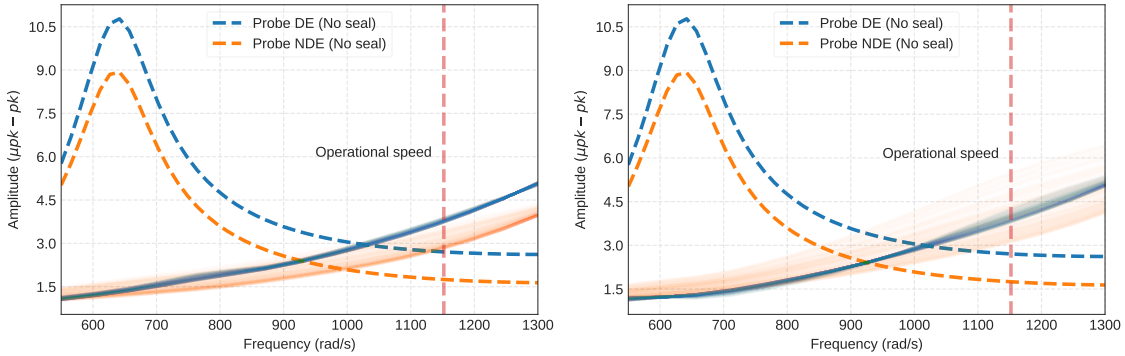

(a) $L = 95$ and $c = 1.5$.

(b) $L = 95$ and $c = 3.5$.

(c) $L = 65$ and $c = 1.5$.

(d) $L = 65$ and $c = 3.5$.

Figure 4.21: Stochastic analysis for the unbalance response with different values of L and c (no seal condition plotted as dashed lines for refference).

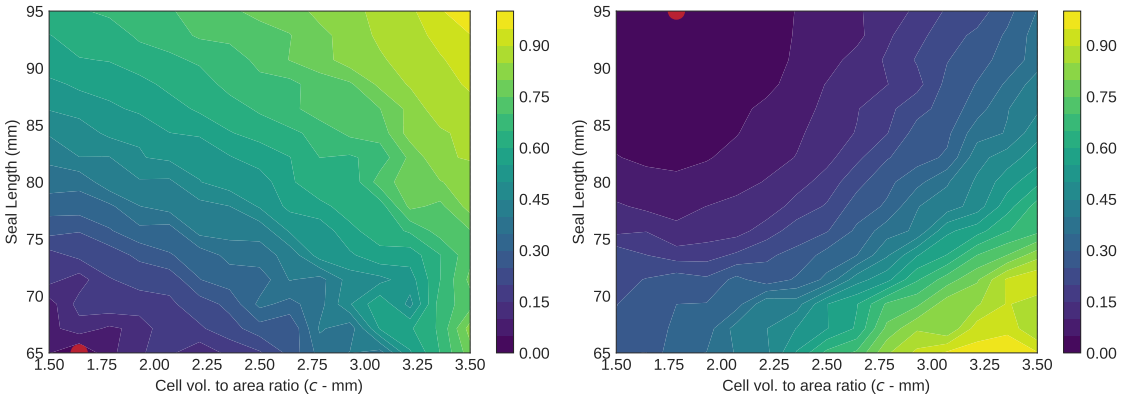

(a) f_2 mean - μ_2.

(b) f_2 variance - ${\sigma^2}_2$.

Figure 4.22: Surfaces for objective f_2 - log dec at the operating speed. For the mean, the minimum values in this case represent points where the log decrement is higher, which is the desired optimization.

unbalance response at four different pair of values for L and c. The results are shown in fig. 4.21, where the amplitude values for the unbalance response with no seals (dashed line) is plotted for reference. In the figure there is an indication for the operational speed (1152 rad/s)

As we can see, fig. 4.21c presents the optimum result for the amplitude mean and variance. The amplitude mean is lower in this case due to the reduced stiffness that affects the natural frequency position and mode shape, therefore affecting the unbalance response. Another important point is that for these values of L and c the damping is also higher. A more general explanation regarding the effects of L and c on the stiffness and damping will be discussed later.

Figure 4.21b shows the results with values of $L = 95$ and $c = 3.5$. In this case the increase in the mean amplitude value can be attributed basically to the change of the natural frequency position and mode due to the increase in stiffness. The variance is also higher and this can be attributed to the stochastic model applied, since the 'vendor' stiffness is always scaled by the ISOTSEAL stiffness.

We evaluated the results for the log decrement, which are presented in fig. 4.22. We can see that the minimum value for the optimization function, which in this case represents the highest log decrement, is also close to the edge where $L = 65$ and $c = 1.5$. This is a consequence of the high damping around these values of L and c.

To evaluate these results, the log decrement distribution for different values of L and c is presented in fig. 4.23. We can see that the log dec for $L = 65$ and $c = 3.5$ (fig. 4.23c) has a higher variance.

To help the evaluation of the log dec variance, the Campbell diagrams for different values of L and c are shown in fig. 4.24. A higher variance for values close of $L = 65$ and $c = 3.5$ is due to the fact that in some cases the lower value for the log

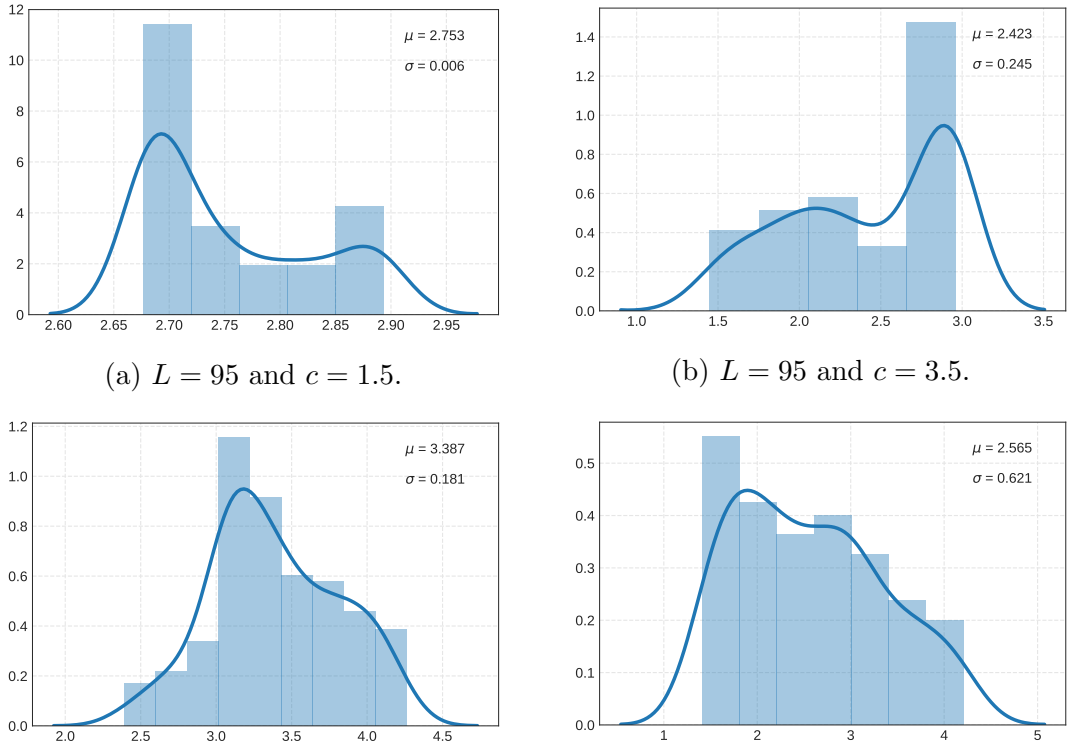

(a) $L = 95$ and $c = 1.5$.

(b) $L = 95$ and $c = 3.5$.

(c) $L = 65$ and $c = 1.5$.

(d) $L = 65$ and $c = 3.5$.

Figure 4.23: Log decrement distribution for different values of L and c.

decrement will be linked to the first mode and in others to the second mode.

Results for the seal leakage are presented in fig. 4.25. The seal leakage does not change with the cell volume to area ratio. MIGLIORINI *et al.* [5] evaluates three seal with different hole depths. Their calculation for the seal leakage with the bulk-flow model also shows the same leakage for the three seals, independent of the hole depth. This is explained by the fact that in the model of KLEYNHANS and CHILDS [41] the zeroth-order equations are independent of hole depth, since in this equation there is no perturbation in the eccentricity and $V = 0$. The only parameter that can change the leakage dependence on hole depth is the friction factor, which in this work is kept constant. MIGLIORINI *et al.* [5] also keeps the friction factor constant.

In reality the leakage will change with the hole-depth, as shown in experiments carried out by CHILDS *et al.* [53]. MIGLIORINI *et al.* [5] CFD results show that the surface streamlines along the seal are influenced by the vortex formation in the hole. The vortex shape was affected by the hole depth which influenced the resistance felt by the jet flow in the clearance region, resulting in a change of the leakage.

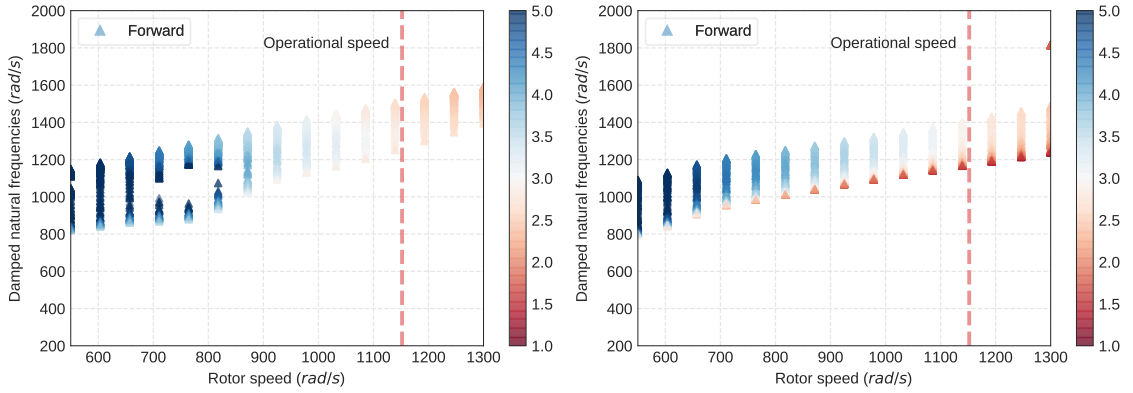

(a) $L = 95$ and $c = 1.5$.

(b) $L = 95$ and $c = 3.5$.

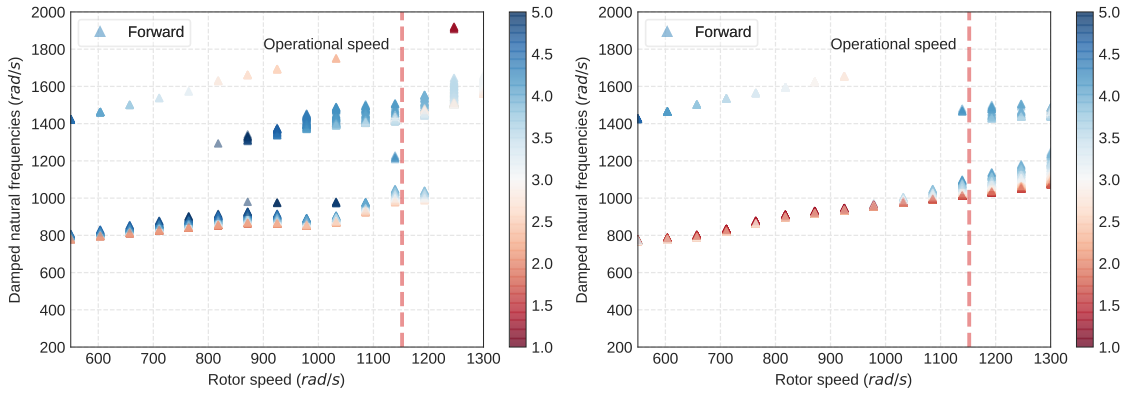

(c) $L = 65$ and $c = 1.5$.

(d) $L = 65$ and $c = 3.5$.

Figure 4.24: Stochastic analysis for the Campbell diagram with different values of L and c.

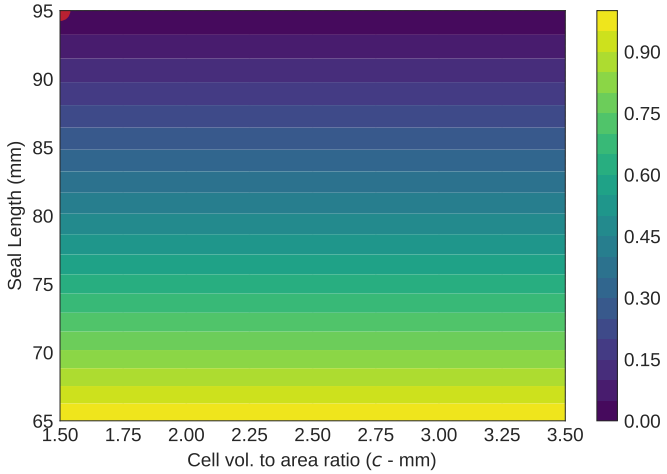

Figure 4.25: Seal leakage - μ_3.

4.4 Stiffness and Damping Dependence on L and c

The purpose of this section is to explain how stiffness and damping vary with the seal length - L, and the cell area to volume ratio - c.

To evaluate this dependence the same range of values for L and c used in the robust optimization analysis are used here to generate surfaces that show the values for each dynamic coefficient.

As explained earlier the effective stiffness and damping can be calculated as:

$$K_{eff} = (K(\Omega) + \Omega c(\Omega))A \qquad \text{(eq. (3.57) revisited)}$$

$$C_{eff} = (C(\Omega) - \frac{k(\Omega)}{\Omega})A \qquad \text{(eq. (3.58) revisited)}$$

We will use these equations to group the results that will be presented next.

Figure 4.26 shows the results for the direct stiffness and the cross-coupled damping multiplied by the precession Ω. We can see that the direct stiffness is one order of magnitude greater than the cross-coupled damping multiplied by Ω. This means that the effective stiffness is basically not affected by the cross-coupled damping as we can see in fig. 4.27.

Results show that the K_{eff} increases with the seal length. This is explained by the fact that the stiffness is calculated by integrating the pressure along the z direction, so if we increase the length K_{eff} is also increased.

The dependency of the stiffness to the cell volume to area ratio, and therefore to the cell depth - H_d, is more complex. As explained by KLEYNHANS and CHILDS [41], the cells of the seal act to reduce the effective acoustic velocity of flow through the seal, which can drop the seal acoustic natural frequency.

The effective acoustic velocity for the seal is calculated with

$$c_0 = \sqrt{\frac{Z_c R_g T}{1 + \frac{H_d}{H}}} \tag{4.8}$$

where Z_c is the gas compressibility, R_g is the gas constant and T is the temperature. Therefore, the effective acoustic velocity is a function of the ratio between cell depth and clearance - H_d/H.

In the work of MIGLIORINI *et al.* [5] three seals with only different hole-depth are compared. The stiffness coefficients for these seals calculated with ISOTSEAL are reproduced here in fig. 4.28. As we can see, in lower frequencies we have the stiffness increasing with the hole-depth, but in high frequencies the behavior is the opposite.

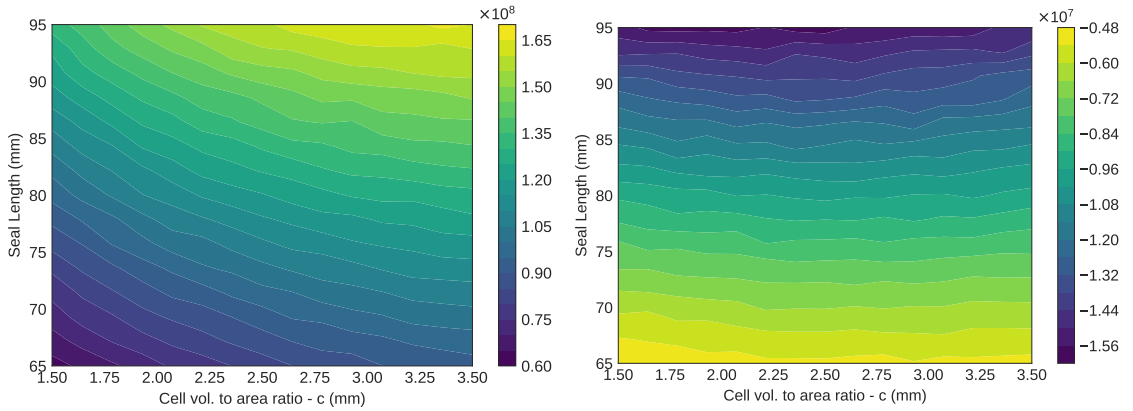

(a) Direct stiffness (K_{xx}). (b) Cross coupled damping times Ω (ΩC_{xy}).

Figure 4.26: Direct stiffness (K_{xx}) and cross-coupled damping (C_{xy}) mean value at operating speed.

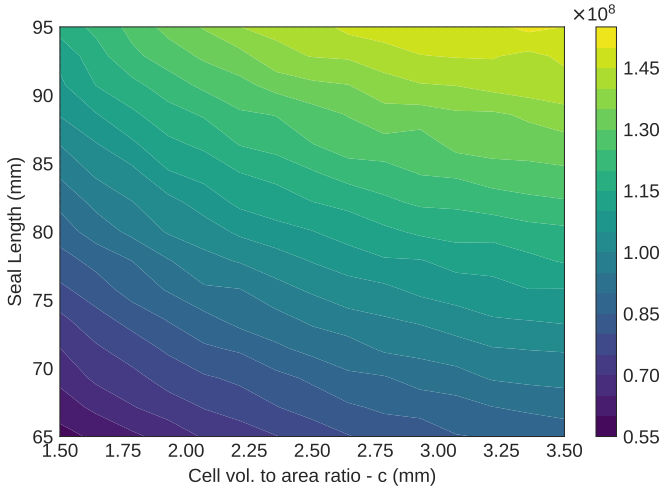

Figure 4.27: Effective stiffness - K_{eff}.

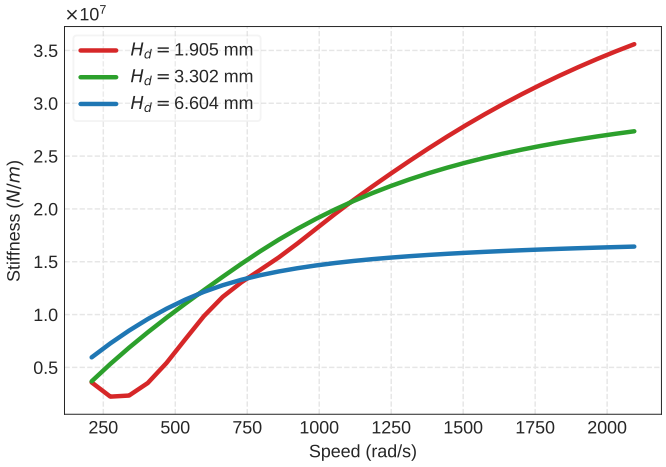

Figure 4.28: Direct stiffness for seals with different hole-depths.

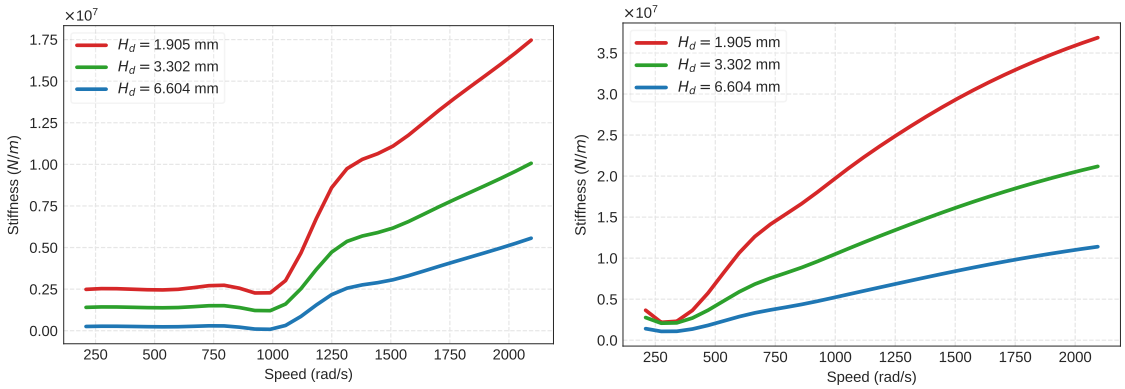

(a) $H_d/H = 5$. (b) $H_d/H = 10$.

Figure 4.29: Seals presented in the work of MIGLIORINI *et al.* [5] but with the same relation H_d/H.

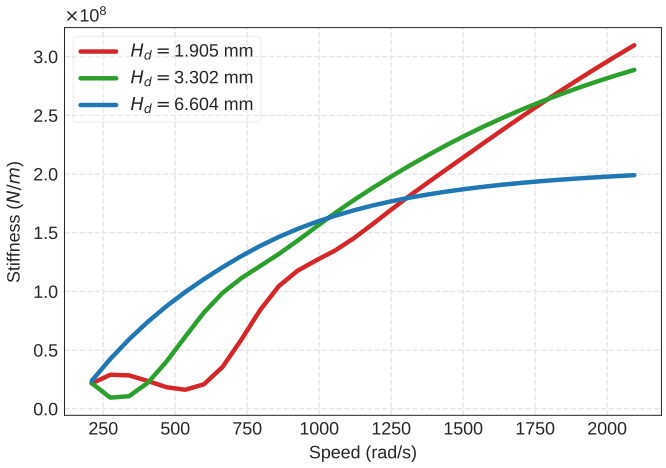

Figure 4.30: Effective damping - C_{eff}.

If we do a comparison by changing the clearance to keep the same relation H_d/H for the three seals, and therefore the same effective acoustic velocity we have the results shown in fig. 4.29. In this case, the lines do not intercept and we have a more clear relation between H_d and the stiffness.

In the current work, the seal clearance does not change. Therefore we need to know, regarding the acoustic effects, in which region we are operating. To do this, we will show, for the seal and operational conditions used in the current work, what is the stiffness coefficient when we consider the hole-depth used in the previous example. The results are presented in fig. 4.30, and we can notice that for our operational speed (1152 rad/s) the lower hole-depth presents a reduced stiffness. So we can see that results presented in fig. 4.27 are coherent since we are operating at a frequency where the effective acoustic velocity of the seal has an impact.

For the damping, results are presented in fig. 4.32.

As the effective stiffness, the effective damping is also increased by increasing

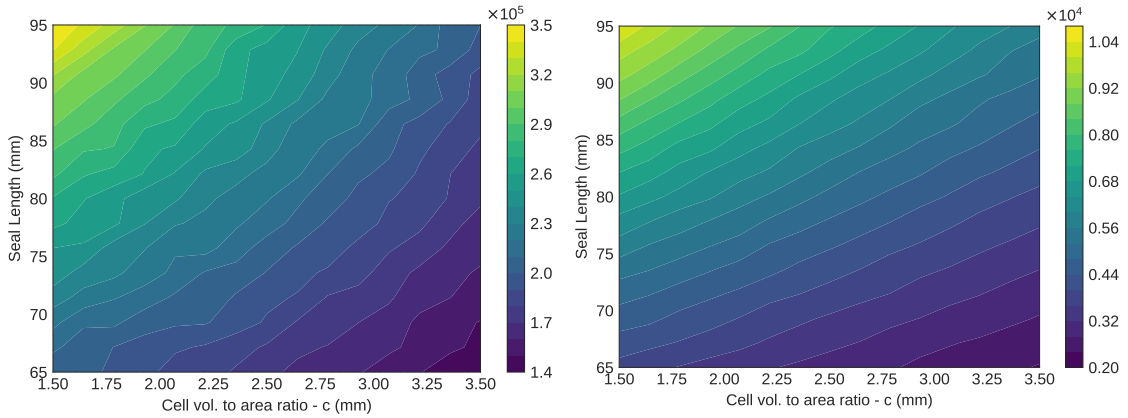

(a) Direct damping (C_{xx}). (b) Cross coupled stiffness per Ω ($\frac{K_{xy}}{\Omega}$).

Figure 4.31: Direct damping (C_{xx}) and cross-coupled stiffness (C_{xy}) mean value at operating speed.

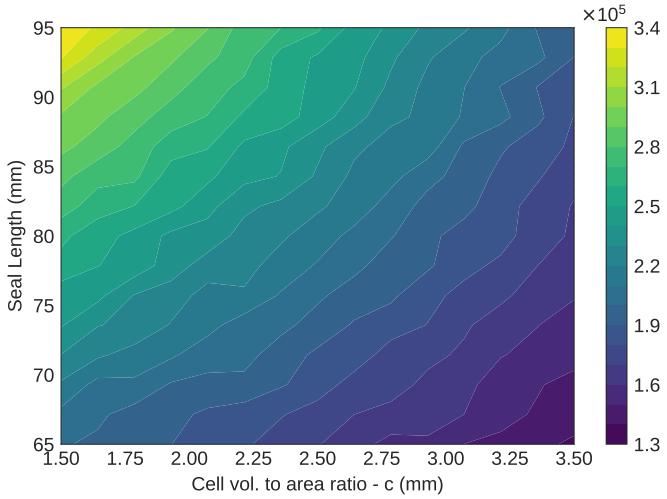

Figure 4.32: Effective damping - C_{eff}.

the seal length - L. Differently to other seals, where the tangential velocity will increase as the fluid progresses in the axial direction, in the damper seal the swirl of the fluid is decreased at the entrance and its value is kept low throughout the seal. This justifies the increase in damping when L is increased.

Chapter 5

Conclusions

A stochastic model which considers the uncertainties in the damper seal model has been proposed to evaluate how these uncertainties impact the rotordynamic behavior.

We have evaluated the critical speed map (Campbell diagram) and the results show that the uncertainties in this component modeling can have a considerable impact on natural frequencies position and log decrement. All evaluated cases show a much higher log decrement than the value of 0.1 required by the current standards.

The unbalance response has been changed when compared to the 'no seal' condition. The change in the natural frequency positions, damping factors, and mode shapes are responsible for this change in the unbalance response. The change in the mode shapes is particularly important since this can change the balancing condition obtained during the high-speed balance that is conducted without the seal in no load conditions.

A robust optimization has been carried out to evaluate how the seal design could be improved to optimize the following specific objectives:

- $f_1(L, c)$ evaluates the vibration amplitude at the non-drive-end side probe at operating speed;
- $f_2(L, c)$ evaluates the lowest logarithmic decrement between the first and second forward mode at operating speed. We choose these modes because they are the closest to the operating speed and the forward mode is the one that will become unstable with a high cross-coupled stiffness;
- $f_3(L, c)$ evaluates the mass leakage for the seal at operating speed.

This optimization suggests that the seal performance regarding the rotordynamic coefficients could be improved by decreasing the hole depth and the seal length. We have found a more robust solution with a higher length. However, given that with

this higher length the log decrement is at minimum above 2.6, which is a very conservative value when compared with the standard required value of 0.1, the use of this design may not be justified.

5.1 Future Work

The analysis carried out in this work considered that the bearing coefficients remain constant. However, the seal has such a high stiffness that it can move the shaft position and alter the bearing coefficients. An iterative process may be necessary to incorporate this in the current analysis.

The stochastic model and the robust optimization are costly in computational terms. The application of different sampling methods could be applied to decrease the time needed to carry out an analysis.

The software used to calculate the damper seal coefficients (ISOTSEAL) considers the ideal gas equation of state. The gas used in this work cannot be considered ideal, due to the high pressure and high CO2 content. The implementation of a seal model considering a real gas equation of state would help to diminish the uncertainties within the model.

Other types of probability distribution could be considered to incorporate the model uncertainties better. Data from experiments could be a source to determine which distribution should be used.

The damper seal coefficients are highly dependent on the compressor operational conditions. Other analysis regarding the uncertainties in these operational parameters could be carried out to evaluate how this component can affect the equipment in off-design conditions.

5.2 Reproducibility

All the developed code used in this dissertation is available at the following on-line repository, except for small scripts used to treat and organize data and some files.

https://github.com/raphaeltimbo/ross

The last commit to the repository before the issue of this document has the following hash:

```
commit 7c62530701af74e119dbdbe5fef0fae74f2da867
```

Unfortunately the complete reproduction of the work is compromised due to the use of some proprietary software such as XLTRC2 (used to validate the developed code) and ISOTSEAL (used to calculate the damper seal coefficients).

Bibliography

[1] API 617, A. . "API 617, 2014", *Axial and Centrifugal Compressors and Expander-Compressors" Eighth Edition, American Petroleum Institute, Washington, DC*, 2014.

[2] FRISWELL, M. I. *Dynamics of rotating machines*. Cambridge University Press, 2010.

[3] VON PRAGENAU, G. L. "Damping seal for turbomachinery". out. 8 1985. US Patent 4,545,586.

[4] KLEYNHANS, G. F. *A two-control-volume bulk-flow rotordynamic analysis for smooth-rotor/honeycomb-stator gas annular seals*. Tese de Doutorado, Texas A&M University, 1996.

[5] MIGLIORINI, P. J., UNTAROIU, A., WOOD, H. G. "A Numerical Study on the Influence of Hole Depth on the Static and Dynamic Performance of Hole-Pattern Seals", *Journal of Tribology*, v. 137, n. 1, pp. 011702, 2015.

[6] LÜDTKE, K. H. *Process centrifugal compressors: basics, function, operation, design, application*. Springer Science & Business Media, 2013.

[7] VANNINI, G., CIONCOLINI, S., CALICCHIO, V., et al. "Development of a High Pressure Rotordynamic Test Rig for Centrifugal Compressors Internal Seals Characterization". In: *Proceedings of the Fortieth Turbomachinery Symposium, Houston, TX, September*, pp. 12–15, 2011.

[8] CHILDS, D. W., VANCE, J. M. "Annular gas seals and rotordynamics of compressors and turbines". In: *Proceedings of the 26th Turbomachinery Symposium*, pp. 201–220, 1997.

[9] NORONHA, R. F. D., UJIHARA, D. Y., REZENDE-TAPAJOZ, L. D., et al. "Applying CFD to Solve a Vibration Problem of a Compressor". In: *Proceedings of the 44th Turbomachinery Symposium*. Turbomachinery Laboratories, Texas A&M Engineering Experiment Station, 2015.

[10] VANNARSDALL, M. L. *Measured Results For A New Hole-Pattern Annular Gas Seal Incorporating Larger Diameter Holes, Comparisons To Results For A Traditional Hole-Pattern Seal, And Predictions*. Tese de Mestrado, Texas A&M University, 2011.

[11] GEARY JR, C. H., DAMRATOWSKI, L. P., SEYER, C. H., et al. "Design and Operation of the WorldTs Highest Pressure Gas Injection Centrifugal Compressors". In: *Offshore Technology Conference*. Offshore Technology Conference, 1976.

[12] VON PRAGENAU, G. L. "Damping seal for turbomachinery", *Marshall Space Flight Center, Huntsville, AL, NASA TP-1987*, 1982.

[13] CHILDS, D., ELROD, D., HALE, K. "Annular honeycomb seals: Test results for leakage and rotordynamic coefficients; comparisons to labyrinth and smooth configurations", *Journal of Tribology*, v. 111, n. 2, pp. 293–300, 1989.

[14] HA, T. W., CHILDS, D. W. "Friction-factor data for flat-plate tests of smooth and honeycomb surfaces", *Journal of tribology*, v. 114, n. 4, pp. 722–729, 1992.

[15] HOLT, C. G., CHILDS, D. W. "Theory versus experiment for the rotordynamic impedances of two hole-pattern-stator gas annular seals", *Journal of tribology*, v. 124, n. 1, pp. 137–143, 2002.

[16] CHILDS, D. W., WADE, J. "Rotordynamic-Coefficient and Leakage Characteristics for Hole-Pattern-Stator Annular Gas Seals—Measurements Versus Predictions", *Journal of tribology*, v. 126, n. 2, pp. 326–333, 2004.

[17] WAGNER, N. G., STEFF, K., GAUSMANN, R., et al. "Investigations on the dynamic coefficients of impeller eye labyrinth seals". In: *Proceedings of the Thirty-Eighth Turbomachinery Symposium, Houston, TX, September*, pp. 14–17, 2009.

[18] VANNARSDALL, M., CHILDS, D. W. "Static and Rotordynamic Characteristics for a New Hole-Pattern Annular Gas Seal Design Incorporating Larger Diameter Holes", *Journal of Engineering for Gas Turbines and Power*, v. 136, n. 2, pp. 022507, 2014.

[19] KOCUR, J. A., NICHOLAS, J. C., LEE, C. C. "Surveying tilting pad journal bearing and gas labyrinth seal coefficients and their effect on rotor stability". In: *36th Turbomachinery Symposium, Turbomachinery Laboratory, Texas A&M University, College Station, TX, September*, pp. 10–13, 2007.

[20] ISO 1940, S. "Mechanical Vibration-Balance Quality Requirements of Rigid Rotors", *Part I: Determination of Permissible Residual Unbalance,*, 1998.

[21] INMAN, D. J. *Engineering vibration*. Pearson; 4 edition, 2013.

[22] RONDON, D. *Thrust gas bearing analytical tool development*. Tese de Mestrado, NTNU, 2014.

[23] BALDASSARRE, L., FULTON, J. W. "Rotor Bearing Loads with Honeycomb Seals and Volute Forces in Reinjection Compressors". In: *Proceedings of the Thirty-Sixth Turbomachinery Symposium*, pp. 11–20, 2007.

[24] BALDASSARRE, L., BERNOCCHI, A., FAILLI, L., et al. "Honeycomb seal effect on rotor response to unbalance". In: *Proceedings of the Forty-Third Turbomachinery Symposium, Houston, TX, Sept*, 2014.

[25] BALDASSARRE, L., FONTANA, M., BERNOCCHI, A., et al. "Effect Of Relative Journal Bearing And Honeycomb Seal Direct Stiffness On Radial Synchronous Vibrations Of High-Pressure Centrifugal Compressors". In: *Proceedings of the 45th Turbomachinery Symposium*. Texas A&M University. Turbomachinery Laboratories, 2016.

[26] API 684, A. . "API 684, 2005", *Tutorial on Rotordynamics: Lateral Critical, Unbalance Response, Stability, Train Torsional and Rotor Balancing," Second Edition, American Petroleum Institute, Washington, DC*, 2005.

[27] COWPER, G. "The shear coefficient in Timoshenko's beam theory", *Journal of applied mechanics*, v. 33, n. 2, pp. 335–340, 1966.

[28] HE, M. "Thermoelastohydrodynamic analysis of fluid film journal bearings." 2004.

[29] BLACK, H. "Effects of hydraulic forces in annular pressure seals on the vibrations of centrifugal pump rotors", *Journal of Mechanical Engineering Science*, v. 11, n. 2, pp. 206–213, 1969.

[30] CHILDS, D. W. "The Space Shuttle Main Engine High-pressure Fuel Turbopump Rotordynamic Instability Problem", *Journal of Engineering for Power*, v. 100, n. 4, pp. 48–57, 1978.

[31] BLACK, H., ALLAIRE, P., BARRETT, L. "Inlet Flow Swirl in Short Turbulent Annular Seal Dynamics". In: *Proceedings of the Ninth International Conference in Fluid Sealing*, pp. 1–3, 1981.

[32] CHILDS, D. W. *Turbomachinery rotordynamics: phenomena, modeling, and analysis*. John Wiley & Sons, 1993.

[33] CHILDS, D. W. "Dynamic analysis of turbulent annular seals based on Hirs' lubrication equation", *Journal of lubrication technology*, v. 105, n. 3, pp. 429–436, 1983.

[34] HIRS, G. "A bulk-flow theory for turbulence in lubricant films", *Journal of Lubrication Technology*, v. 95, n. 2, pp. 137–145, 1973.

[35] NELSON, C. "Rotordynamic coefficients for compressible flow in tapered annular seals", *Journal of Tribology*, v. 107, n. 3, pp. 318–325, 1985.

[36] ELROD, D., NELSON, C., CHILDS, D. "An Entrance Region Friction Factor Model Applied to Annular Seal Analysis: Theory Versus Experiment for Smooth and Honeycomb Seals", *Journal of tribology*, v. 111, n. 2, pp. 337–343, 1989.

[37] HA, T. W., CHILDS, D. "Annular Honeycomb-Stator Turbulent Gas Seal Analysis Using a New Friction-Factor Model Based on Flat Plate Tests", *Journal of tribology*, v. 116, n. 2, pp. 352–359, 1994.

[38] HA, T., MORRISON, G., CHILDS, D. "Friction-factor characteristics for narrow channels with honeycomb surfaces", *Journal of tribology*, v. 114, n. 4, pp. 714–721, 1992.

[39] SCHARRER, J. "Discussion:"Annular Honeycomb-Stator Turbulent Gas Seal Analysis Using a New Friction-Factor Model Based on Flat Plate Tests"(Ha, TW, and Childs, DW, 1994, ASME J. Tribol., 116, pp. 352–359)", *Journal of Tribology*, v. 116, n. 2, pp. 359–359, 1994.

[40] SCHARRER, J. K. "Theory versus experiment for the rotordynamic coefficients of labyrinth gas seals: part I—a two control volume model", *Journal of Vibration, Acoustics, Stress, and Reliability in Design*, v. 110, n. 3, pp. 270–280, 1988.

[41] KLEYNHANS, G. F., CHILDS, D. W. "The acoustic influence of cell depth on the rotordynamic characteristics of smooth-rotor/honeycomb-stator annular gas seals". In: *ASME 1996 International Gas Turbine and Aeroengine Congress and Exhibition*, pp. V005T14A017–V005T14A017. American Society of Mechanical Engineers, 1996.

[42] NELSON, C. "Analysis for leakage and rotordynamic coefficients of surface-roughened tapered annular gas seals", *ASME J. Eng. Gas Turbines Power*, v. 106, n. 4, pp. 927–934, 1984.

[43] MIGLIORINI, P. J., UNTAROIU, A., WOOD, H. G., et al. "A computational fluid dynamics/bulk-flow hybrid method for determining rotordynamic coefficients of annular gas seals", *Journal of Tribology*, v. 134, n. 2, pp. 022202, 2012.

[44] JAYNES, E. T. *Probability theory: the logic of science*. Cambridge university press, 2003.

[45] BOYD, S., VANDENBERGHE, L. *Convex optimization*. Cambridge university press, 2004.

[46] BEYER, H.-G., SENDHOFF, B. "Robust optimization–a comprehensive survey", *Computer methods in applied mechanics and engineering*, v. 196, n. 33-34, pp. 3190–3218, 2007.

[47] ZANG, C., FRISWELL, M., MOTTERSHEAD, J. "A review of robust optimal design and its application in dynamics", *Computers & structures*, v. 83, n. 4-5, pp. 315–326, 2005.

[48] RITTO, T., LOPEZ, R., SAMPAIO, R., et al. "Robust optimization of a flexible rotor-bearing system using the Campbell diagram", *Engineering Optimization*, v. 43, n. 1, pp. 77–96, 2011.

[49] WALT, S. V. D., COLBERT, S. C., VAROQUAUX, G. "The NumPy array: a structure for efficient numerical computation", *Computing in Science & Engineering*, v. 13, n. 2, pp. 22–30, 2011.

[50] JONES, E., OLIPHANT, T., PETERSON, P. "{SciPy}: open source scientific tools for {Python}", 2014.

[51] HUNTER, J. D. "Matplotlib: A 2D graphics environment", *Computing in science & engineering*, v. 9, n. 3, pp. 90–95, 2007.

[52] CONSORTIUM, T. R. "XLTRC2 Rotordynamics Software Suite (2002)", *Turbomachinery Laboratory, Texas A&M University, College Station, TX*, 2002.

[53] CHILDS, D. W., ARTHUR, S., MEHTA, N. J. "The Impact of Hole Depth on the Rotordynamic and Leakage Characteristics of Hole-Pattern-Stator Gas Annular Seals", *Journal of Engineering for Gas Turbines and Power*, v. 136, n. 4, pp. 042501, 2014.

Appendix A

Rotor geometry

.

Table A.1 shows the shaft elements table.

Table A.1: Shaft elements

	n	L	i_d	o_d	E	G_s	rho
0	0.0	0.0355	0.1409	0.1510	2.0684e+11	8.2737e+10	7833.4128
1	1.0	0.0360	0.1409	0.1510	2.0684e+11	8.2737e+10	7833.4128
2	2.0	0.0540	0.0000	0.0800	2.0684e+11	8.2737e+10	7833.4128
4	3.0	0.0430	0.0000	0.0800	2.0684e+11	8.2737e+10	7833.4128
5	4.0	0.0165	0.0000	0.0880	2.0684e+11	8.2737e+10	7833.4128
6	5.0	0.0070	0.0000	0.0880	2.0684e+11	8.2737e+10	7833.4128
7	6.0	0.0070	0.0000	0.0880	2.0684e+11	8.2737e+10	7833.4128
8	7.0	0.0365	0.0000	0.0900	2.0684e+11	8.2737e+10	7833.4128
9	8.0	0.0510	0.0000	0.0900	2.0684e+11	8.2737e+10	7833.4128
11	9.0	0.0250	0.0000	0.1030	2.0684e+11	8.2737e+10	7833.4128
12	9.0	0.0250	0.1030	0.1380	6.8947e+03	6.8947e+03	7833.4128
13	10.0	0.0160	0.0000	0.0850	2.0684e+11	8.2737e+10	7833.4128
14	10.0	0.0160	0.0850	0.1380	6.8947e+03	6.8947e+03	7833.4128
15	11.0	0.0242	0.0000	0.1040	2.0684e+11	8.2737e+10	7833.4128
16	11.0	0.0242	0.1040	0.1740	6.8947e+03	6.8947e+03	7833.4128
17	12.0	0.0045	0.0982	0.1740	6.8947e+03	6.8947e+03	7833.4128
18	12.0	0.0045	0.0000	0.0982	2.0684e+11	8.2737e+10	7833.4128
19	13.0	0.0125	0.1040	0.1740	6.8947e+03	6.8947e+03	7833.4128
20	13.0	0.0125	0.0000	0.1040	2.0684e+11	8.2737e+10	7833.4128
21	14.0	0.0200	0.0000	0.1060	2.0684e+11	8.2737e+10	7833.4128
22	14.0	0.0200	0.1060	0.1840	6.8947e+03	6.8947e+03	7833.4128
23	15.0	0.0627	0.0000	0.1080	2.0684e+11	8.2737e+10	7833.4128

Table A.1: Shaft elements

	n	L	i_d	o_d	E	G_s	rho
24	15.0	0.0627	0.1080	0.1840	6.8947e+03	6.8947e+03	7833.4128
25	16.0	0.0380	0.0000	0.1100	2.0684e+11	8.2737e+10	7833.4128
26	16.0	0.0380	0.1100	0.1840	6.8947e+03	6.8947e+03	7833.4128
27	17.0	0.0380	0.0000	0.1220	2.0684e+11	8.2737e+10	7833.4128
28	17.0	0.0380	0.1220	0.1390	6.8947e+03	6.8947e+03	7833.4128
29	18.0	0.0300	0.0000	0.1350	2.0684e+11	8.2737e+10	7833.4128
30	18.0	0.0300	0.1350	0.1750	6.8947e+03	6.8947e+03	7833.4128
31	19.0	0.0530	0.1177	0.1965	6.8947e+03	6.8947e+03	7833.4128
32	19.0	0.0530	0.0000	0.1177	2.0684e+11	8.2737e+10	7833.4128
33	20.0	0.0194	0.0000	0.1223	2.0684e+11	8.2737e+10	7833.4128
34	20.0	0.0194	0.1223	0.1270	6.8947e+03	6.8947e+03	7833.4128
35	21.0	0.0135	0.0000	0.1223	2.0684e+11	8.2737e+10	7833.4128
36	21.0	0.0135	0.1223	0.1270	6.8947e+03	6.8947e+03	7833.4128
38	22.0	0.0495	0.0000	0.1177	2.0684e+11	8.2737e+10	7833.4128
39	23.0	0.0195	0.0000	0.1223	2.0684e+11	8.2737e+10	7833.4128
40	23.0	0.0195	0.1223	0.1270	6.8947e+03	6.8947e+03	7833.4128
41	24.0	0.0124	0.0000	0.1223	2.0684e+11	8.2737e+10	7833.4128
42	24.0	0.0124	0.1223	0.1270	6.8947e+03	6.8947e+03	7833.4128
44	25.0	0.0490	0.0000	0.1177	2.0684e+11	8.2737e+10	7833.4128
45	26.0	0.0197	0.1223	0.1270	6.8947e+03	6.8947e+03	7833.4128
46	26.0	0.0197	0.0000	0.1223	2.0684e+11	8.2737e+10	7833.4128
47	27.0	0.0123	0.0000	0.1223	2.0684e+11	8.2737e+10	7833.4128
49	27.0	0.0123	0.1223	0.1270	6.8947e+03	6.8947e+03	7833.4128

Table A.1: Shaft elements

	n	L	i_d	o_d	E	G_s	rho
50	28.0	0.0495	0.0000	0.1177	2.0684e+11	8.2737e+10	7833.4128
51	29.0	0.0198	0.0000	0.1223	2.0684e+11	8.2737e+10	7833.4128
52	29.0	0.0198	0.1223	0.1270	6.8947e+03	6.8947e+03	7833.4128
53	30.0	0.0116	0.0000	0.1223	2.0684e+11	8.2737e+10	7833.4128
54	30.0	0.0116	0.1223	0.1270	6.8947e+03	6.8947e+03	7833.4128
56	31.0	0.0495	0.0000	0.1177	2.0684e+11	8.2737e+10	7833.4128
57	32.0	0.0199	0.1223	0.1270	6.8947e+03	6.8947e+03	7833.4128
58	32.0	0.0199	0.0000	0.1223	2.0684e+11	8.2737e+10	7833.4128
59	33.0	0.0120	0.0000	0.1223	2.0684e+11	8.2737e+10	7833.4128
61	33.0	0.0120	0.1223	0.1270	6.8947e+03	6.8947e+03	7833.4128
62	34.0	0.0495	0.0000	0.1177	2.0684e+11	8.2737e+10	7833.4128
63	35.0	0.0201	0.0000	0.1223	2.0684e+11	8.2737e+10	7833.4128
64	35.0	0.0201	0.1223	0.1270	6.8947e+03	6.8947e+03	7833.4128
65	36.0	0.0124	0.0000	0.1223	2.0684e+11	8.2737e+10	7833.4128
66	36.0	0.0124	0.1223	0.1270	6.8947e+03	6.8947e+03	7833.4128
68	37.0	0.0570	0.0000	0.1177	2.0684e+11	8.2737e+10	7833.4128
69	38.0	0.0260	0.0000	0.1350	2.0684e+11	8.2737e+10	7833.4128
70	38.0	0.0260	0.1350	0.1750	6.8947e+03	6.8947e+03	7833.4128
71	39.0	0.0380	0.0000	0.1220	2.0684e+11	8.2737e+10	7833.4128
72	39.0	0.0380	0.1220	0.1390	6.8947e+03	6.8947e+03	7833.4128
73	40.0	0.0380	0.0000	0.1100	2.0684e+11	8.2737e+10	7833.4128
74	40.0	0.0380	0.1100	0.1840	6.8947e+03	6.8947e+03	7833.4128
75	41.0	0.0627	0.0000	0.1080	2.0684e+11	8.2737e+10	7833.4128
76	41.0	0.0627	0.1080	0.1840	6.8947e+03	6.8947e+03	7833.4128
77	42.0	0.0200	0.0000	0.1060	2.0684e+11	8.2737e+10	7833.4128
78	42.0	0.0200	0.1060	0.1840	6.8947e+03	6.8947e+03	7833.4128
79	43.0	0.0125	0.0000	0.1040	2.0684e+11	8.2737e+10	7833.4128
80	43.0	0.0125	0.1040	0.1740	6.8947e+03	6.8947e+03	7833.4128
81	44.0	0.0045	0.0982	0.1740	6.8947e+03	6.8947e+03	7833.4128
82	44.0	0.0045	0.0000	0.0982	2.0684e+11	8.2737e+10	7833.4128
83	45.0	0.0242	0.1040	0.1740	6.8947e+03	6.8947e+03	7833.4128
84	45.0	0.0242	0.0000	0.1040	2.0684e+11	8.2737e+10	7833.4128
85	46.0	0.0160	0.0000	0.0850	2.0684e+11	8.2737e+10	7833.4128
86	46.0	0.0160	0.0850	0.1380	6.8947e+03	6.8947e+03	7833.4128
87	47.0	0.0250	0.0000	0.1030	2.0684e+11	8.2737e+10	7833.4128

Table A.1: Shaft elements

	n	L	i_d	o_d	E	G_s	rho
88	47.0	0.0250	0.1030	0.1380	6.8947e+03	6.8947e+03	7833.4128
89	48.0	0.0510	0.0000	0.0900	2.0684e+11	8.2737e+10	7833.4128
90	49.0	0.0505	0.0000	0.0900	2.0684e+11	8.2737e+10	7833.4128
92	50.0	0.0181	0.0000	0.0900	2.0684e+11	8.2737e+10	7833.4128
93	51.0	0.0181	0.0000	0.0900	2.0684e+11	8.2737e+10	7833.4128
94	52.0	0.0363	0.0000	0.0900	2.0684e+11	8.2737e+10	7833.4128
95	53.0	0.0135	0.0000	0.0900	2.0684e+11	8.2737e+10	7833.4128
96	54.0	0.0350	0.0900	0.2450	6.8947e+03	6.8947e+03	7833.4128
97	54.0	0.0350	0.0000	0.0900	2.0684e+11	8.2737e+10	7833.4128
98	55.0	0.0240	0.0000	0.0872	2.0684e+11	8.2737e+10	7833.4128
99	55.0	0.0240	0.0872	0.1120	6.8947e+03	6.8947e+03	7833.4128
100	56.0	0.0320	0.0000	0.0850	2.0684e+11	8.2737e+10	7833.4128
101	56.0	0.0320	0.0850	0.1130	6.8947e+03	6.8947e+03	7833.4128

Table A.2: Disk elements.

	n	Mass	Ip	It
4	4	15.12	0	0
5	22	6.90999	0.0469997	0.0249998
6	25	6.92999	0.0469997	0.0249998
7	28	6.94999	0.0479997	0.0249998
8	31	6.97999	0.0479997	0.0249998
9	34	6.93999	0.0479997	0.0249998
10	37	6.95999	0.0479997	0.0249998